Astronomy & Astrophysics manuscript no. aa6035-06
October 20, 2006

Solar CIV vacuum-ultraviolet Fabry-Perot interferometers

G. A. Gary[1], E. A. West[1], D. Rees[2], J. A. McKay[3], M. Zukic[4], and P. Herman[5]

[1] National Space Science and Technology Center (NSSTC), Marshall Space Flight Center (MSFC), Huntsville, AL, 35812, USA
e-mail: Allen.Gary@nasa.gov
[2] Hovemere Ltd., Sevenoaks, Kent, TN145HD, UK
e-mail: Hovemere@yahoo.co.uk
[3] Remote Sensor Concepts, Washington, D. C., 20010, USA
e-mail: Jack.McKay@verizon.net
[4] Cascade Optical Corporation, Santa Ana, CA, 92705, USA
e-mail: MZukic@c-optical.com
[5] Department of Electrical and Computer Engineering, University of Toronto, Toronto, Ontario, M5S-3G4, Canada
e-mail: HermanP@ecf.utoronto.ca

Received 13 July 2006 / Accepted 23 September 2006

ABSTRACT

Aims. A tunable, high spectral resolution, high effective finesse, vacuum ultraviolet (VUV) Fabry-Perot interferometer (FPI) is designed for obtaining narrow-passband images, magnetograms, and Dopplergrams of the transition region emission line of CIV (155 nm).

Methods. The integral part of the CIV narrow passband filter package (with a 2–10 pm *FWHM*) consists of a multiple etalon system composed of a tunable interferometer that provides high-spectral resolution and a static low-spectral resolution interferometer that allows a large effective free spectral range. The prefilter for the interferometers is provided by a set of four mirrors with dielectric high-reflective coatings. A tunable VUV piezoelectric-control interferometer has undergone testing using the surrogate F_2 eximer laser line at 157 nm for the CIV line. We present the results of these tests with a description of the overall concept for a complete narrow-band CIV spectral filter. The static interferometer of the filter will be built using a set of fixed MgF_2 plates. The four-mirror prefilter is designed to have dielectric multilayer Π-stacks employing the concept used in the Ultraviolet Imager of NASA's Polar Spacecraft. A 10-pm dual etalon system allows the effective free spectral range to be commensurate with the prefilter profile. With an additional etalon, a triple etalon system would allow a spectrographic resolution of 2 pm. The basic strategy has been to combine the expertise of spaceflight etalon manufacturing with VUV coating technology to build a VUV FPI which combines the best attributes of imagers and spectrographs into a single compact instrument.

Results. High spectral-resolution spectro-polarimetry observations of the transition region CIV emission can be performed to increase our understanding of the magnetic forces, mass motion, evolution, and energy release within the solar atmosphere at the base of the corona where most of the magnetic field is approximately force-free. The 2D imaging of the full vector magnetic field at the height of maximum magnetic influence (minimum plasma beta) can be accomplished, albeit difficult, by measuring the Zeeman splitting of the CIV resonance pair. Designs of multiple VUV FPIs can be developed for integration into future orbiting solar observatories to obtain rapid cadence, spectral imaging of the transition region.

Key words. Sun: transition region – Sun: UV radiation – instrumentation: interferometers – space vehicles: instrument – techniques: spectroscopic

1. Introduction

1.1. Scientific rational

Within solar physics and astrophysics, a major goal is to understand the magnetic forces, evolution, and energy release within the solar and stellar atmospheres. Events from the sun drives space weather which has significant influences on our technologically-dependent society and space initiatives. The observation and analysis of the transition region (TR, the interface between the chromosphere and the corona) is important in the physical understanding of the solar atmosphere and its ubiquitous magnetic field. The ultraviolet resonance emission lines of CIV (~155 nm) are formed in the middle of the TR at a temperature of 100 000 K. A CIV narrow-passband filter will provide critical instrumentation for these solar TR observations. Using this filter with a polarimeter, the magnetic structure, mass motion, and morphology within the transition region can be studied. Although difficult, the measurement of the full vector magnetic field at the height of maximum magnetic influence (minimum plasma beta) can be accomplished by measuring the Zeeman splitting of the CIV resonance pair. Previous observations of this doublet resonance line have either been with scanning spectrographs or broadband filters with their inherent limitations in simultaneity and spectral purity.

We present the design of a multiple-etalon vacuum-ultraviolet Fabry-Perot interferometer (VUV FPI) which can be integrated within the future orbiting solar observatories. The VUV FPI combines the best attributes of a spectrograph and an imager in a compact and versatile instrument. The instrument reported here shows the proof-of-concept of a high-spectral-resolution, high-finesse VUV FPI for obtaining narrow-passband images, magnetograms, and Dopplergrams of CIV. (Finesse is defined by the ratio of the free spectral range (FSR) to the spectral resolution (full-width at half maximum, $FWHM$)).

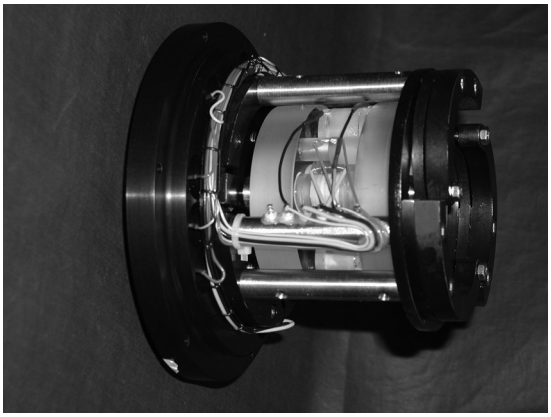

Fig. 1. Internal view of the MSFC/Hovemere CIV scanning FPI which incorporates (Cascade Optical Corporation) VUV coating technology with a resolving power of 22,100. This could be used as one element for the high resolution interferometer for a multiple Fabry-Perot etalon spectral filter for CIV described in the text. The interferometer length is 150 mm.

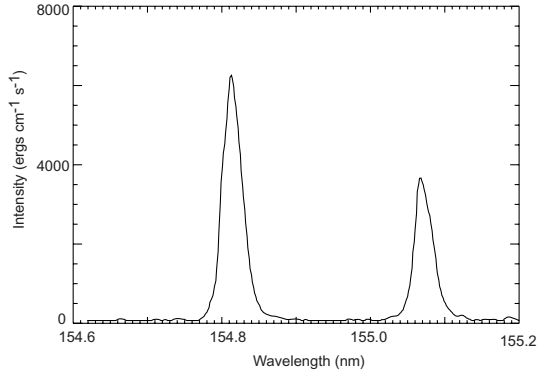

Fig. 2. The CIV resonance line pair at 154.82 nm and 155.08 nm showing the 1 to 2/3 ratio in peak intensity. The NRL HRTS (21 July, 1975) active region scan is plotted at 1.5 pm steps.

We further present two complete design concepts for the CIV narrow passband filter with a spectral resolution of $\Delta\lambda$ = 10 pm and 2 pm *FWHM* and a resolving power of $\lambda/\Delta\lambda$ = 15 500 and 77 500, respectively. The dual etalon system ($\Delta\lambda$ = 10 pm) consisting of three sub-elements: (1) a scanning high-resolution interferometer (HRI) providing a high-resolution passband, (2) a static (fixed gap) low-resolution interferometer (LRI) providing the system with a larger effective free spectral range (*FSR*), and (3) four reflective interference filters performing as a prefilter. A triple system ($\Delta\lambda$ = 2 pm) would have an additional HRI. The test results of the Marshall Space Flight Center's (MSFC) 10 pm HRI are given in Sect. 4 for the piezoelectric-controlled etalon (Fig. 1). The prefilter design, composed of four mirrors with dielectric multilayer stacks, follows the coating design of the orbiting Ultraviolet Imager (UVI) (Zukic et al. 1993). A two etalon design allows the effective free spectral range to be commensurate with the prefilter spectral width as described below.

The spectral filter system can provide a 3D data cube that combines a 2D field of view with non-sequential spectral scanning at selective steps through the lines of CIV. The multiple etalon Fabry-Perot filter systems described here are designed specifically for the transition region CIV emission line pair at 154.821/155.077 nm ($2s^2S_{\frac{1}{2}}$–$2p^2P^\circ_{1\frac{1}{2}}$ / $2s^2S_{\frac{1}{2}}$–$2p^2P^\circ_{\frac{1}{2}}$) (Fig. 2). This strong CIV resonance line pair, associated with 10^4K plasma at an effective parallel-atmosphere height of 2000 km (Fig. 3), is Zeeman sensitive with effective Lande-g values of $g_{\rm eff}$ = 1.167/$g_{\rm eff}$ = 1.333, and has a profile half-width of 130–275 pm (Peter 2002). For a magnetic field strength of 1000G, the Zeeman splitting is 0.15 pm for 155.08 nm. Because of the small splitting, Stokes polarimetric scans of the line are employed to derive the magnetic field. The CIV characteristics and spectral purity provide important line diagnostics for analysis of the transition region. With high throughput, narrow-band spectral imagery offers the advantage of avoiding spectrographic rastering and allows precise and simultaneous 2D context imaging. The observation of the highly dynamic, non-equilibrium thermodynamic transition region of the solar atmosphere requires rapid 3D-imaging spectrometry and magnetography. These short dynamic time scales are ∼10 s for CIV waves (DeForest 2005), 120 s for blinkers (Madjarska & Doyle 2000), 200 sec for coronal loop oscillations (De Pontieu et al. 2003), and a few minutes for spicules (Xia et al. 2004). For example, the plasma sprays or spicules rise up from the photosphere through the chromosphere into the transition region (TR) along flux tubes as extremely inhomogeneous and dynamic small-scale activity. Assuming an appropriate size telescope, the non-sequential stepping pattern of a filter with a minimum number of steps provides a rapid cadence compatible with these events. Such small-scale dynamics in the lower solar atmosphere is related to coronal heating, convection, waves, and mass loss. For another example of the dynamics of the TR, rapid magnetic reconnection has been associated with both types of CIV brightenings: the impulsive brightenings (without line broadenings and near magnetic inversion lines) and the explosive events (with line broadenings and associated with weak magnetic fields) (Porter et al. 1987; Porter & Dere 1991; Dere et al. 1991; Chae et al. 1998).

From the photosphere to the transition region, the plasma beta parameter (β, the ratio of the gas pressure to the magnetic pressure) decreases by a factor $\sim 10^4$ (Gary 2001). The Alfven wave velocity increases by a factor of $\sim 10^2$ inferring a significant decrease in the response time to magnetic reconnection events. For a third example of the rapid variability of the TR, recent Fourier analysis of the CIV TRACE data has weakly indicated waves in the 100 mHz (10s period) range, coming possibly from small-scale reconnection or chromospheric shocks (DeForest 2004). Insight into the basic mechanism responsible for these fundamental solar phenomena requires specific diagnostic techniques to refine and infer the physical properties of this region. Such systematic and random velocity fields broaden and shift the line profile. Observing the upward propagation of mechanical energy and its dissipation is key to understanding the energy balance of the solar atmosphere. A high-throughput VUV FPI can provide rapid 3D-imaging spectroscopy that is needed to understand the overall physics, such as, (i) the dissipation of mechanical energy carried upward from the convection zone and dissipation of energy stored in the magnetic field, (ii) the regime and location of each kind of heating, (iii) the complex velocity field in the transition region, (iv) the role of the magnetic field in heating at various heights, and (v) the distinctive structures of the transition region. A CIV VUV FPI can provide images, Doppler velocities, and magnetic field measurements simultaneously for correlation studies and analysis. In a recent review of the solar atmosphere, Solanki & Hammer (2001) stated that the transition region between the chromosphere and the corona is the most fascinating part of the solar atmosphere because of the thin thermal interface. They further point out that because of the spatial and temporal scales of the region, TR observations will

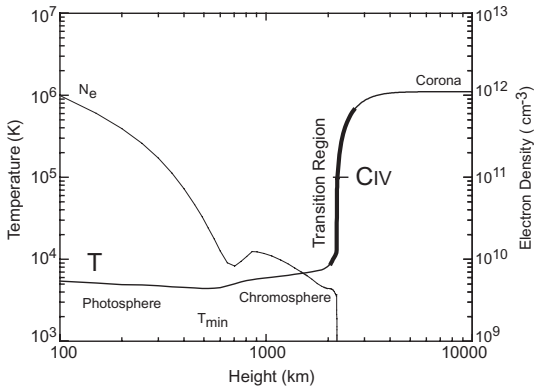

Fig. 3. The spectral lines of CIV are formed in the logarithmic middle of the temperature range of the transition region (after Peter 2001). As a function of height, the temperature is increasing rapidly through the transition region and the density is decreasing.

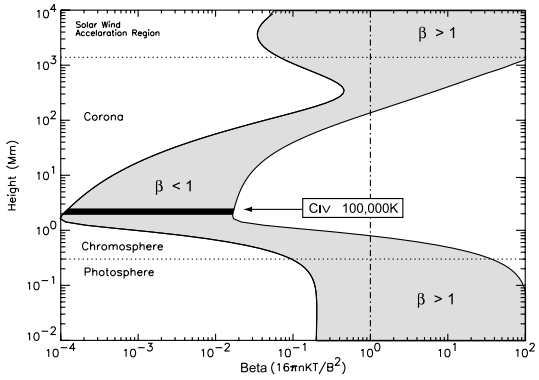

Fig. 4. Plasma Beta plot showing that CIV emission coming from the minimum value of beta. (Gary 2001).

require the highest demands on the spectral, spatial, and temporal resolutions for future space missions.

Recent observations have revealed significant spatial correlations of the CIV emission with the highly redshifted fibril or spicule-like structures in Hα. De Pontieu and Tarbell reported recently that this correlation promises to shed light on the long outstanding issue of what role chromospheric spicule-like jets play in the heating and momentum balance of the outer atmosphere (De Pontieu & Tarbell 2002). Also using broadband images of Transition Region and Coronal Explorer (TRACE), Tarbell, Handy, & Judge (1999) report that bright CIV transients are seen associated with flux emergence and cancellation, and can be associated with high-velocity explosive events seen in Solar Ultraviolet Measurement of Emitted Radiation's (SUMER) spectra. The CIV emission can be well-separated from the photospheric magnetic footpoints, suggesting that it takes place on current sheets higher in the atmosphere separating different flux systems. However, they report that the CIV emission of moss regions (foot points of hot coronal loops) is contrasted with that of similar plage which does not have hot loops above it. Hence improved narrow passband imaging of CIV is one step to better understand coronal heating.

Fundamentally, a VUV imaging spectral filter can provide information on the three important physical processes: the magnetic field topology, the coronal process, and the dynamics of the atmosphere. The magnetic field in the region where the ratio (β) of plasma pressure to magnetic pressure is low, where flares and coronal mass ejections (CMEs) are believed to be triggered, can be directly measured using the VUV FPI (Moore & Sterling 2005). The force-free fields in the transition region may undergo large changes in direction where the magnetic field is within the low-β region (Fig. 4). Then extrapolation upward through the rest of the corona would give us a better calculation of the dynamic magnetic field in this region, and would be related to the evolution and interaction with the interplanetary medium.

The understanding of the exact mechanisms leading to the heating of the solar corona is still an enigma. However, the related activities are characterized by a spatial-temporal intermittent brightness of the solar atmosphere. The role of thermal conduction in the energy redistribution of the coronal through the transition region needs to be understood to resolve the coronal heating problem. Generally the heating models are hydrodynamic mechanisms with shock dissipation of acoustic waves or magnetic heating mechanisms subdivided into electric-magnetic wave (alternating current) or stress (direct current) mechanisms with numerous dissipation processes possible (e.g. shocks, Laudau damping, resonance absorption, turbulent heating, and anomalous heating). In all these processes the energy must pass through the transition region. Hence, the TR analysis of the intensity variations, the magnetic fields, and the profile variations will help to unravel the coronal heating processes.

The position and structure of the transition region is problematic due to the dynamics of time-varying heating along a magnetic field line, the small and large-scale restructuring of the magnetic field (reconnection and electric currents), the small and large mass ejections (spicules and CMESs), and oscillations/waves. Improved observations of transition region variability (e.g., blinklers, nano-flares, and microflares) will help define the fine structure dynamics that transfers the photospheric convectional energy into the corona. The dynamics of the structure is clearly seen in the CIV of HRTS spectrograms and the SOHO/SUMER limb images (see Figs. 5 and 6). HRTS's Doppler shifts over sunspots reveal down flows of up to 150 km s^{-1}.

Peter and his colleagues in a number of recent articles have emphasized the importance of the transition region and CIV characteristics (Peter 2000, 2001). Gontikakis, Peter, & Dara (2003), have studied the CIV line broader tail component, whose origin is unclear. They found that the size of the bright radiance features is always larger than the size of the structures of the Dopplergrams and Doppler widths. The network features seem to diminish at a temperature around 10^5 K due to the thermodynamic properties of the transition region, and the mean size of the structures of the tail component radiance is smaller than the one of the core radiance. On-disk observations by SUMER show that the lower transition region ($2\times10^4 - 2\times10^5$ K) is composed of small loops and knots of emission and thread-like structures (Feldman et al. 1999); hence the complex structure of the transition remains to be deciphered and requires new instrumentation.

For example, a specific observing program would study the rapid variation of transition region structures to investigate the injection of material and wave into the corona. The FPI spectral stability in tuning to a series of nearby chromospheric lines provides the absolute velocities. Rapid scanning over the FOV gives small scale velocity variations of filaments, surges, and spicules and gives k-ω diagrams for wave and shock analysis within the TR.

With these reasons for studying the CIV emission, the following section discusses the design, development, and testing of a CIV interferometer capable of meeting the rapid tuning,

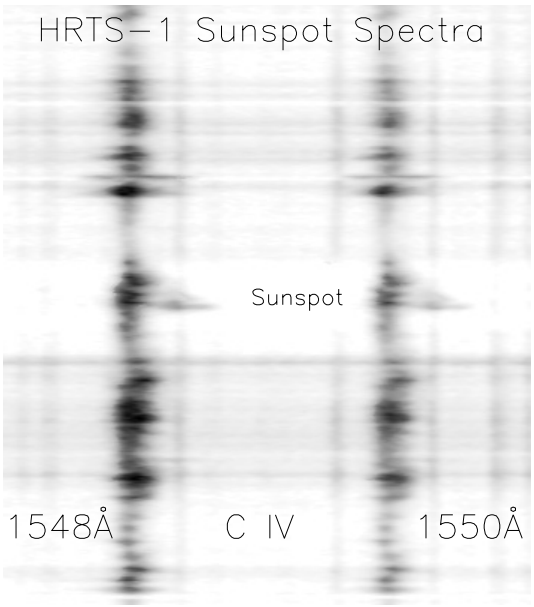

Fig. 5. HRTS spectrum of the two CIV resonance lines showing velocity mirco-structures. (After Dere et al. 1982).

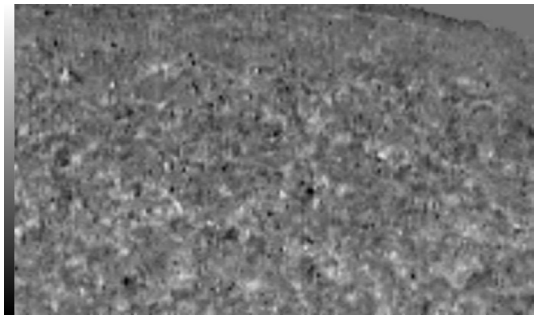

Fig. 6. A SOHO/SUMER Dopplergram of CIV showing the Doppler micro-structure of the transition region as compared to the size of the intensity structures (After Dammasch et al. 1999). The limb is seen in the upper right hand corner. The scale on the far left is ± 20 km s^{-1} (white = red shifted).

high spectral resolution, and imaging requirements. With some loss in transmission, improvement in the spectral resolution, by a third etalon, would allow for analysis of the line asymmetries and small scale spectral anomalies. However, a dual etalon interferometer can focuse on high cadence Dopplergraphy. We will discuss both configurations. First, however, prior attempts at the construction of CIV interferometer are discussed in the next secion; all these prior etalons had relatively large passbands (300–2000 pm).

1.2. Background and Related Work

1.2.1. Fabry-Perot interferometry

In a series of papers in the 1970's, Bideau-Méhu and colleagues reported on their investigation of Fabry-Perot interferometry in the vacuum ultraviolet (Guern et al. 1974, Bideau-Méhu et al 1976, Bideau-Méhu 1980). By 1980, they were employing 11 mm thick, 50 mm diameter, $\lambda/80$ MgF_2 plates and Al-MgF_2 films (22 nm–5 nm) to achieve reflecting finesse of 6.7 but only a peak transmission of 9% at 152 nm. This resulted in a free spectral range of $FSR = 6.44$ nm with a full width at half maximum of $FWHM = 1.89$ nm. The defect finesse derived from the flatness should have given a finesse of 11. Inferior plate performance was probably the cause of lower finesse. A recent VUV etalon development program (1996–2000) was performed by the Lockheed-Martin Solar and Astrophysics Laboratory (LMSAL) group and colleagues that resulted in two articles directly related to the discussion here (Bruner et al. 1997; Wülser et al. 2000). The first paper reported on the theoretical finesse and transmission of the etalon in the VUV. It demonstrated that a 155 nm etalon *predicted* reflectance finesse could be 34 with a transmission of 36%. A study of an optimized Π-interference coating (see Sect. 3.2) for a 155 nm etalon predicted a transmittance of 5.3% with a peak reflectance of 91% with 3.5% absorption but had a high out-of-band response to the blue. The second paper on Fabry-Perot etalons reported on construction attempts in the vacuum ultraviolet region (120–150 nm). The LMSAL group noted that the performance of the high-efficiency coatings required by a UV etalon is limited both by the availability of suitable coating materials, and by the uniformity and accuracy of the deposition process. A vacuum-spaced etalon with cultured quartz plates was operated at 169.5 nm with a low finesse of 4. In this LMSAL study, a 140 nm FPI without Π-interference coating, was constructed with transmittance of 3%, $FSR = 3.4$ nm, finesse = 10.5, and $FWHM$ $\Delta\lambda = 0.32$ nm. Led by Zukic, the LMSAL and the MSFC UVI teams have investigated a family of coating designs based on the fluoride salts of magnesium and lanthanum, finding that a practical etalon performance may be achievable at wavelengths as short as 120 nm (e.g., Zukic 1998). While the lack of UV transmitting materials with a wide range of refractive index is problematic, the concern can be overcome by using a vacuum-spaced etalon design with MgF_2 and LaF_3-based coatings. LMSAL efforts did produce a tunable etalon but did not use capacitive sensor feedback circuitry, but used a manual method to scan in wavelength. Because of the lack of other efforts and the scientific potential of CIV interferometry, we have extended their efforts and report our findings here.

1.2.2. Related spectroscopy

Because of the minimum progress in VUV interferometers, the observations of the solar transition region within the past 10 years have been limited to broad passband imagers and spatial-scanning spectrographs (Table 1). However, these instruments have demonstrated the extensive scientific interest in the transition region. In particular, on the disk, CIV measurements have been performed with (i.) the orbiting TRACE having a 3.7 nm-*FWHM* spectral filter with a 2.4% transmission with an additional cleaning filter (at 160 nm, 16.6%), (ii.) SUMER using an area scanning spectrograph with 4–8 pm resolution, (iii.) HRTS having 5 pm resolution, and (iv.) MSSTA, the Stanford University's sounding rocket Multi-Spectral Solar Telescope Array, having a CIV broadband filter of 10 nm *FWHM*. The Naval Research Laboratory's (NRL) Very high Angular resolution ULtraviolet Telescope (VAULT) is also a spectroheliograph rocket payload and has a passband of 7 pm which is the predecessor of HRTS (Korendyke et al. 2001; Bartoe et al. 1977). A MSFC sounding rocket's Solar Ultraviolet Magnetograph Investigation (SUMI) is to measure the TR's CIV at 2 pm spectral resolution. SUMI, in part, has evolved from the 1980's UVSP SMM high spectral resolution (2–4 pm) but SUMI will have a higher polarimetric resolution of CIV (West et al. 2000, 2001). SUMER is a normal incidence spectrometer with ~8 pm resolution at 160 nm. A full disk CIV scan with a spatial resolution of ~1 arcsec took over a day to scan the sun; a typical

Table 1. Transition Region Observing Instruments (100–200 nm).

Instruments [a]	Type	Wavelength [nm]	$\Delta\lambda$ [pm]	Δx [arcsec]	Science	FOV [arcsec]	Status
Sounding Rockets							
SUMI	Spectrograph	155 & 280	2 & 5	1	Magnetography	180	Under Construction
HRTS	Spectrograph	120-170	5	1	Line profiles	1000	Flown
VAULT	Spectrograph	120-120	7	0.3	Line profiles	3600	Flown
MSSTA	Imager	155+14λ's	10 nm	1	Multiple λ's	2000	Flown
Orbiting Missions							
SUMER	Spectrograph	39-161	4-8	1.5	Line profiles	300	On orbit
UVCS	Spectrograph	49-150	9-14	7	Coronal lines	300	On orbit
TRACE	Imager	155, 160, 170 + 4λ's	3.7 nm	1	Multiple λ's	510	On orbit
AIA	Imager	160, 170 + 8λ's	20 nm	1	Multiple λ's	2460	Under Construction

[a] Notation: SUMI= Solar Ultraviolet Magnetograph Instrument (MSFC); HRTS=High Resolution Spectrograph (NRL); VAULT=Very high Angular resolution Ultraviolet Telescope (NRL); MSSTA=Multi-Spectral Solar Telescope Array(Stanford); SUMER=Solar Ultraviolet Measurements of Emitted Radiation (SOHO/Lindau); UVCS=Ultraviolet Coronal Spectrometer (SOHO/CfA); TRACE=Transition Region and Coronal Explorer (SMEX/LMSAL); AIA=Atmospheric Imaging Assembly (SDO/LMSAL); $\Delta\lambda$ = spectral resolution, Δx = spatial resolution.

active region scan of CIV of 5×5 arcmin^2 at 2arcsec spatial resolution requires ~13 min with 4.2 pm/pixel. This slowness exemplifies difficulties of a spectrograph for capturing the rapidly changing TR.

The current orbiting imager of the transition region is TRACE which images the solar corona and transition region at high angular and temporal resolution. Its VUV wavelengths are 121.6 (8 nm, 14% transmittance), 155.0 (3.7 nm 2.4%), 160.0 (24.5 nm, 16.5%), and 170.0 nm (20 nm, 24.5%). The TRACE telescope uses four normal-incidence coatings for the EUV-VUV on quadrants of the primary mirrors. The broadband 160 nm response has shown great sensitivity to transient events which relates to the rapid thermal conduction in the transition region. Under construction, the Solar Dynamics Observatory's Atmospheric Imaging Assemble (SDO/AIA) will characterize the dynamic evolution of the solar plasma from the chromosphere to the corona, and will follow the connection of plasma dynamics with *photospheric* magnetic activity throughout the solar atmosphere but again with a broad passband transition region filter at 160 nm with 20 nm *FWHM*. Although the capture rate is moderate, ~4 fpm, the spectral profile includes many lines and provides only intensity data.

For CIV, these high-speed imagers and high-spectral resolution spectrographs can be combined into a single, compact filtergraph by employing a VUV FPI. This would fill the void that is seen in both the near-term orbiting observatories, AIA and Solar-B, by extending high spectral resolution into the transition region and permit exploration of the minimum plasma beta region.

1.3. The rational

These instruments show that a spectral resolution of ~2–10 pm produces important scientific returns and that a prefilter of ~3–4 nm (cf. TRACE) can be manufactured (Handy et al. 1998). Therefore, as a needed alternative to the standard use of a VUV spectrograph, the specification for a multiple etalon interferometer is given. The CIV VUV FPI will have the capability of extending the TR research by supplying a filtergraph to the present arsenal in a compact volume for orbiting missions. The etalon system would allow imaging a large field of view at specific wavelengths and enable the design of either a 10 pm filter-type magnetograph or a 2 pm spectro-polarimetric- type of magnetograph. For a spectral resolution of $\Delta\lambda/\lambda$, the FOV is given by FOV ~ $(8\Delta\lambda/\lambda)^{1/2}(A_{\rm etalon}/A_{\rm telescope})$ where $A_{\rm etalon}$ and $A_{\rm telescope}$ are the apertures of the etalon and telescope, respectively. For $A_{\rm etalon}$ = 25 mm, $A_{\rm telescope}$ = 300 mm, $\Delta\lambda = 2$ pm and $\lambda = 155$ nm, the FOV is ~4 arcmin and would allow the imaging of over 73% of active regions on the sun (Tang et al. 1984). The instrument concepts outlined here are based on having one or two of the etalons tunable with an additional fixed-gap etalon. The fixed-gap (static) etalon is used to isolate a single order of the tunable etalon and is commensurate with a 3.5 nm VUV prefilter (see Hernandez 1986, Chap. 4, for discussion of multiple etalon devices). This fixed-gap etalon acts to span the spectral blocking requirements between the narrower VUV filter in the 155 nm range and the FSR of the double configuration. The double (or triple) configuration is designed to give a bandpass of 10 pm (or 2 pm) and maximize the suppression of intensity coming from the continuum in the region. Our design focuses on the CIV TR line, which, fortunately, has the molecular fluoride (F_2) laser line of 157 nm nearby which can be used for profiling and aligning the filter in the laboratory. The general VUV technology discussed here can be extended to allow FPIs to be built at the other important solar lines in the VUV (e.g., OV 137 nm, OIV 140 nm, & HeII 164 nm) for extended studies of fine structuresdynamics, density, and temperature.

2. Theory and design

A Fabry-Perot narrow passband filter offers the advantage in that the observer can choose distinct spectral modes depending on what is desired: (i) a rapid-cadence Dopplergraphy, (ii) seven-step filter magnetography, or (iii) full spectral profiling. For spectral polarimetry, the central challenge for a FPI is to acquire the precise Stokes profile in a time that does not exceed the evolutionary timescale of the solar features on minimum angular scales of the instrument (Gary et al. 2006). For the dual etalon system, 5 spectral samples are sufficient to provide Dopplergrams. For the triple etalon system, ~15 samples across the spectral line will provide sufficient details of the line profile. A FPI offers the advantage of avoiding spatial rastering, with the disadvantage of spectral tuning; but the higher throughput and resultant faster cadence, coupled with post-focal image

techniques more than compensate for this disadvantage (Gary et al. 2003). Furthermore, the major advantage for a FPI in a spaceflight instrument, as compared with a grating spectrometer, is in compact volume (∼4X). The other advantages are dual functionality of observing modes, simplicity of design, use of fast and accurate piezoelectric tuning, and high étendue, and relative polarization insensitivity.

Our efforts on a VUV etalon system have been an outgrowth of a MSFC program to build a sounding-rocket VUV spectrograph (i.e., the Solar Ultraviolet Magnetograph Investigation – SUMI). Under this research, a scanning VUV interferometer was manufactured with improved Π-coatings, capacitance stabilized controllers, and the special Hansen mechanical mount technology (Remote Sensor Concepts, MD and Hovemere Ltd., UK). Two pairs of $\lambda/200$ MgF_2 plates were produced under this study. The first pair was coated with a CIV reflective coating (by M. Zukic/Cascade Optical Corporation) and overcoated with Al/Ag to allow a visible test of the final plate flatness for coating effects (plate warping). Through the Galaxy Evolution Explorer (GALEX) mission's VUV coatings (135–175 nm), Cascade gained unique experience on coatings at $\lambda \sim 155$ nm to produce better higher-reflectance, lower-absorption coatings (Jelinsky 2003). Having verified that the coating had no effect on the flatness in the visible, the second pair of plates was coated by Cascade and assembled by Hovemere into a tunable VUV etalon system (etalons, mechanical mount, temperature-controlled housing, and capacitance-stabilized control system). The final assembly was tested in the visible at Hovemere and MSFC, and was tested in the VUV with the 157 nm F_2 laser at the University of Toronto. The details of these tests will be given later in the paper.

2.1. Design considerations

The present section establishes the constraints on the design of the VUV FPI and presents the design specifications for a complete Fabry-Perot filter system. A Fabry-Perot spectral filter system provides (1) the required spectral resolution for high-resolution filter spectral imaging; (2) the high etendue (light throughput) to obtain a sufficient number of spectral samples within the appropriate time periods (i.e., a solar oscillation, a wave period, or the time for motion across a resolution element), and to obtain the required magnetic sensitivity within the timescale of changing solar features; (3) a mechanically and optically simpler design compared to a spectrograph; (4) the rapid, adjustable non-sequential tuning between wavelengths that is required for finding the spectral line center and for adjusting the wavelength setting for Doppler-induced shifts, and (5) spectroscopy for 5–20^+ position Stokes line profiles. We will now consider the components of the specific design rationale: spectral resolution, spectral purity, etendue, spectral range, optical configuration, finesse, and blocking filters.

2.1.1. Spectral resolution

The VUV FPI is designed for high spectral resolution in order to reconstruct an acceptable line profile. To resolve a spectral line with half width of $\delta\lambda_s = 35$ pm, a spectral resolution of $\Delta\lambda \sim 5$ pm is required for ∼15 points across the line profile. For typical TR flows of $V \sim 1$ km s^{-1}, the Doppler shift of the line center is only $\Delta\lambda = \lambda\, V/c = 0.5$ pm. Moreover, the overall spectral resolution obtained depends upon the dynamics of the solar image (rate of scene changes), the Poisson statistics of the measurements (throughput at line depth), and the total time required to obtain the spectral profile (SNR and stepping intervals). Assuming Gaussian shaped line profiles and Possion statistics for the detector, and using 15 points, the uncertainty in the Doppler shift can be estimated by $\delta\Delta\lambda_v = \delta\lambda_s/(S/N)$. Assuming $\delta\lambda_s = 35$ pm for CIV and a signal to noise ratio is $(S/N) = 10^3$, the error in the doppler shift is $\delta\Delta\lambda_v = 0.035$ pm (Hagyard, Gary, & West 1988). This uncertainty in the Doppler shift represents an uncertainty in the velocity of ∼7 m s^{-1}. Theoretical modeling of down flows, flux tubes, and Evershed flows can show strong variations and asymmetries in the Stokes profiles (Borrero et al. 2004). High quality spatio-spectral observations can resolve and test these physical models. However, the spectral resolution of ∼10 pm is sufficient to detect the general line-profile shape observed in the spectra, and the wavelength sampling can be dense enough to determine line center. A minimum of five steps across the spectral line is needed. For detail line profile asymmetries at $\lambda = 155$ nm, spectral resolution of $\Delta\lambda/\lambda \sim 1.29 \times 10^{-5}$ is required which gives $\Delta\lambda = 2$ pm or 18 steps interval across the profile. Gary et al. (2006) give a discussion of the CIV radiometry and polarimetry needed for inverting the Stokes CIV line profiles.

The spectral resolution (i.e. 1/resolving power) depends primarily on the finesse for a single etalon, or the free spectral range for a multiple etalon system (Hernandez 1986; Vaughan 1989). For a *single etalon system*, the spectral resolution is approximately $\Delta\lambda/\lambda \sim \lambda/(F\,2\,d)$, where F is the finesse and d is the etalon gap distance. For a $d \sim 0.2$ mm and $\lambda = 155$ nm, then $\Delta\lambda/\lambda \sim 3.9 \times 10^{-4}/F$; hence, to obtain the 10 pm spectral resolution, the finesse must be $F = 6$. However the FSR for a single etalon is then $FSR = 60$ pm. For a spectral resolution of $\Delta\lambda \sim 2$ pm and for a finesse of $F = 8.6$, we need a larger gap ($d \sim 1$ mm) which gives a smaller free spectral range ($FSR = 12$ pm). Because of the impossibility of manufacturing a compatible interference prefilter for a single etalon to isolate a single order, multiple etalons systems must be employed. For a multiple etalon system the spectral resolution is given by $\Delta\lambda/\lambda \sim FSR_{\min}/(F\lambda)$ where the *minimum FSR of the set* of etalons is used to determine the resolution. The *effective* free spectral range of the multi-etalons in combination, however, can be 10–100 times greater, and compatible with VUV prefilters. For multiple etalons, the effective free spectral range of the system is determined by the set of incommensurable etalon spacings; however, the etalon with the minimum FSR sets the passband. Then for $F = 6$, we cannot obtain a passband of 10 pm and must employ a multiple etalon system.

2.1.2. Spectral purity

For a single, vacuum-gap ($n = 1$) etalon, the Fabry-Perot profile is given by an Airy function and requires a narrow blocking system because of the multiple orders (transmission peaks). Assuming perfect flatness and an incident angle of $\theta = 0$ degrees for the collimated beam, the Airy function for a single etalon transmission profile is given by,

$$T = \left(\Omega^2/(1-R)^2\right) / \left[1 + \left\{4R\sin^2(2\pi nd\cos(\theta)/\lambda)\right\}/(1-R)^2\right]$$

where R is the reflectance, L is the loss of the etalon coating, Ω (=$1 - R + L$) is the intensity transmission coefficient for the coating (Hernandez 1986; Vaughan 1989). The spectral order, m, of a single transmission peak is given by the integer value of $2\,n\,d\cos(\theta)/\lambda$). For low losses, then $\Omega \sim 1 - R$, yeilding

$$T = (1-R)^2\left[1 - 2R\cos(4\pi\, n\, d\cos(\theta)/\lambda) + R^2\right]^{-1}.$$

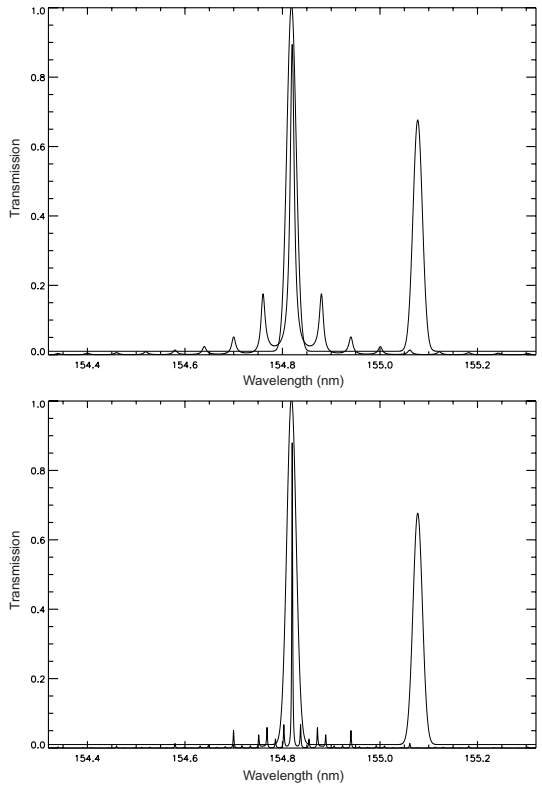

Fig. 7. Plot of the dual (10 pm, *upper panel*) and triple (2 pm, *lower panel*) interferometer transmission profiles (thick line) along with the normalized CIV resonance emission lines at 154.82 and 155.08 nm (thin line). The contamination from the off-band peaks does not affect significiantly the spectral resolution of the CIV lines because of their shifted location and low transmission and because of the weak strength of VUV continuum.

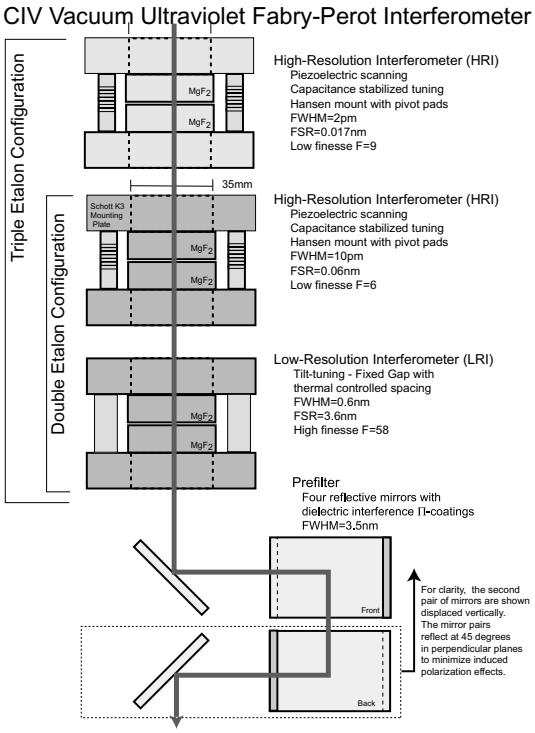

Fig. 8. A schematic of the proposed VUV dual and triple etalon FPI system showing the elements of the system: (HRI), HRI, LRI, and the prefilter. A third etalon (HRI), at the top of the figure, would provide for higher spectral resolution.

For a perfect etalon the transmission is $T_{\max} = 1$ compared to the value of $T_{\max} \sim (1 - L/(1 - R))^2$ for reflections with absorption which are dependent on the loss (L) of the optical coating (Vaughan 1989). For a single Fabry-Perot etalon, the minimum transmission $T_{\min} = (1 - R)^2/(1 + R)^2$ is determined by the reflectance (R) of the coatings of the etalon. For example a single etalon with effective reflectance of $R = 0.77$ (and assuming infinite defect finesse) will have a minimum transmittance of 10^{-2} with respect to the maximum transmittance. The total spectral profile response of a multi-system is determined by the product of the combined etalon profiles. For two identical etalons with $R = 0.77$ the minimum transmittance of 10^{-4} with respect to the maximum transmittance. Tuning the ratio of finesse, the gap distance, and the free spectral range of the individual etalons can optimize the spectral purity, out-of-band rejection and contribution of parasitic orders. Multiple etalon systems have superior out-of-band rejection due to placement of the separate etalon minimums. The transmission of the strongest off-band peaks and the total integrated off-band transmission sets the interferometer specifications for spectral purity. The process involves a tradeoff between the number of etalons and blocking filters. The specific blocking filter characteristics must be enumerated (number, size, types, transmission, and deposition method) to provide the match with the etalons and the physical observations that are to be performed.

Figure 7 shows the resulting transmission profile for both a double and triple etalon system. Superimposed are the dual resonance lines of CIV. It is seen that the double etalon design has higher secondary peaks but since these are outside the CIV line profile these parasitic contributions are small. The double etalon system has a broader *FWHM* since the effective free spectral range must be commensurate with the passband of the prefilter. To improve the passband from 10 pm to 2 pm, an additional tunable etalon is employed and the parasitic contribution is further diminished.

2.1.3. Etendue and finesse

For spectroscopic and polarimetric measurements of rapidly changing physical conditions in the solar atmosphere, the etendue or optical throughput per unit solid angle is a critical design item for the multi-etalon systems. For a single FPI the transmittance is related to the overall finesse and the absorption in the cavity (imperfections and optical absorption). The transmittance goal of the VUV FPI is greater than 50%. Since for a single etalon the maximum and minimum transmittances are functions of the coating reflectivity and losses, the coatings across the operational wavelengths must be specified and compatible with the overall finesse of the etalons. For lower R (which means lower finesse), $T_{\max}$ increases and provides for higher throughput. Hence, a lower finesse is desirable for maximum etendue.

In Fig. 9, for defect-free etalons, the inverse contrast ratio $I_{\min}/I_{\max}$, the maximum transmittance $T_{\max}$, and the reciprocal of the reflectance finesse $1/F_{\rm R}$ is plotted as a function of the etalon coating reflectivity R. We want $I_{\min}/I_{\max}$ to be as small as possible with $T_{\max}$ as large as possible to reduce parasitic noise and maximize throughput. The reflectance finesse $F_{\rm R}$ should also be equal to the defect finesse $F_{\rm D}$. For the selected reflectance of $R = 0.77$, the resulting transmittance is $T_{\max} = 0.76$ and $I_{\min}/I_{\max} = 0.017$.

Because of the etalon surface defects, the actual maximum transmission is dependent on the ratio of the effective finesse

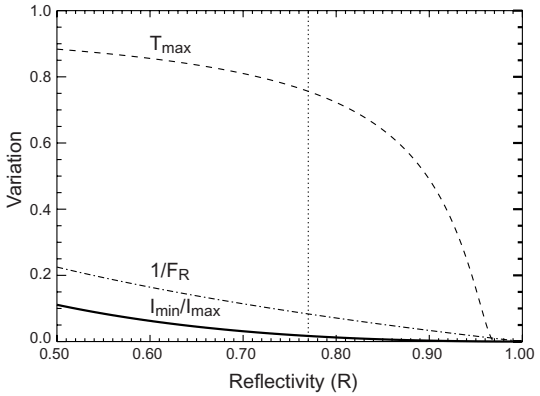

Fig. 9. The variation of $I_{\rm min}/I_{\rm max}$ (solid, lower line), maximum transmittance $T_{\rm max}$ (dashed upper line, $A = 0.03$) and reciprocal reflectance finesse $F_{\rm R}$ (dash-dotted, middle line) vs. the reflectance of the etalon coatings R. The vertical line is at 77% reflectance optimizing for Min($I_{\rm min}/I_{\rm max}$) and Max($T_{\rm max}$).

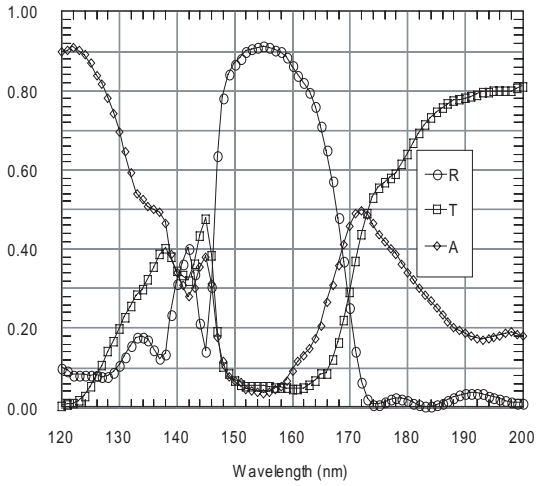

Fig. 10. The reflectance (R), transmittance (T) and absorptance (A, loss) of the Π-multilayer optimized for the mirror coating of the Fabry-Perot etalon operating at ∼155 nm. The multilayer has a peak reflectance of 91.2% at 155 nm. At the same wavelength the multilayer has 5.3% transmittance and 3.5% absorptance (M. Zukic 1999, private communication). This coating will be re-optimize for the static LRI to improve the reflectance to 94.7%.

and the reflective finesse. Reduction of $T_{\rm max}$ is given by $F_{\rm E}/F_{\rm R}$ (McKay 1999). The effective finesse can be estimated by $F_{\rm E} = [F_{\rm R}^{-2} + F_{\rm D}^{-2}]^{-1/2}$. Furthermore, the defect finesse can be approximated by $F_{\rm D} = \lambda/[4\delta_{\rm s}^2 + 22\delta_{\rm rms}^2 + 3\delta_{\rm p}^2]^{1/2}$ where $\delta_{\rm s}$ is the etalon plate spherical deviation from a plane, $\delta_{\rm rms}$ is the plate rms surface roughness, and $\delta_{\rm p}$ is the plate deviation from true parallelism. The root-mean-square defect finesse is generated by surface roughness (irregularities and micro-defects), which are assumed to follow a Gaussian distribution. The parallel finesse is easily achieved by piezoelectric feedback drivers. Hicks et al. (1981) developed a control system that maintains plate parallelism and control spacing to an accuracy better than $\lambda/10\,000$. Therefore the main concern on the etalon optical quality is induced or manufactured warping of the etalon plates. The estimated values of the coefficients are $\delta_{\rm s} = 4$ nm, $\delta_{\rm rms} = 3$ nm, $\delta_{\rm p} = 0$ nm (McKay 1999), Hence, the defect finesse for $\lambda = 155$ is $F_{\rm D} \sim 13$ and since $F_{\rm E}/F_{\rm R} = 1/[1 + F_{\rm R}^2/F_{\rm D}^2]^{1/2}$, this implies $F_{\rm R} < F_{\rm D} = 13$, to insure that the reduction of the maximum transmission is less than $F_{\rm E}/F_{\rm R} > 0.71$. For $R = 0.77$, the condition $F_{\rm R} < F_{\rm D}$ is satisfied since $F_{\rm R} = \pi R^{1/2}/(1 - R) = 12$. The effective finesse is then $F_{\rm E} = [F_{\rm R}^{-2} + F_{\rm D}^{-2}]^{-1/2} = 8.8$ and giving an effective reflectivity of $R_{\rm E} = 0.70$. The ratio G of the maximum transmission to the mean transmission can be approximated by a function of the effective finesse $G \sim 2\,F_{\rm E}/\pi = 5.5$. (McKay 1999). The reduced maximum transmission is $T_{\rm max} = 0.53$, within our goal. The reduced contrast ratio is $I_{\rm min}/\,I_{\rm max} = (1 - R_{\rm E})^2/(1 + R_{\rm E})^2 = 0.031$. Hence, each etalon will have a flatness of $\lambda/200$ at $\lambda = 632.8$ nm (HeNe laser) before coating, and a broadband coating with >70–90% reflectance at 155 ± 5 nm.

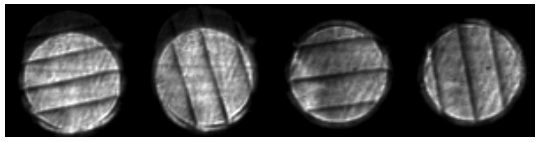

Fig. 11. Interferometry of the 35 mm MgF_2 etalon plates for the VUV Fabry-Perot System with flatness $>\lambda/150$ at 633 nm which is $\lambda/37$ at 155 nm. The first set of the plates were used to verify the Π-coatings and the second set of plates is in the CIV HRI.

The gap distance is the next parameter to be considered. For a peak transmission at wavelength λ, the Airy function gives the etalon gap distance of $d = \lambda\, m/2n$ (Atherton et al. 1981). For a small change in wavelength ϵ_λ, the gap distance must be changed by $\delta d = (\epsilon_\lambda/\lambda)d$. For a fixed gap distance, the spectral distance between the adjacent transmissions orders, i.e., the free spectral range, is $FSR = \lambda^2/2\; n\; d$. For a given order ($m$) and $FSR = 60$ pm, the move to the next transmission peak at 155 nm, i.e., the next order, the gap of d must be moved $\delta d_1 = (FSR/\lambda)d \sim 0.39 \times 10^{-3}$ d. Typically for etalons, the gap distance is $d = 200\ \mu$m and as a result, the piezoelectric stacks must give a tuning range of $\Delta d_{\rm g} \sim \gamma 77$ nm, where γ is the number of free spectral ranges to be scanned. The number γ_{155} (i.e., γ at $\lambda = 155$ nm) must allow wo orders in the visible and to allow the determination of the FSR. For $FSR \sim 60$ pm, the spectral resolution is $\delta\lambda = \gamma\, FSR/2^{12} = 0.3$ pm (e.g. at 155 nm, the equivalent Doppler shift is 0.6 km s^{-1}). The large number (6) for γ_{155} is selected to allow the number of free spectral orders scanned to be ∼2 at the HeNe laser line, 632.8 nm, for testing in the visible. Optical tuning requirements are determined by the need of almost instantaneous stepping to avoid loss of photons and stability of performance. The other factors affecting the tuning are (i) acquisition speed, (ii) stability and control, (iii) repeatability, (iv) PZT feedback systems, (v) thermal compensation, (vi) laser control feedback systems, and (vii) correction of induced temperature and pressure variations within the etalon. The maintenance and tuning of the plate parallelism is solved by capacitance stabilization and piezoelectric driving stacks (Hicks et al. 1984).

As we have discussed, the design of a *single* etalon system needs to have a large separation between orders to allow blocking filters to isolate a particular order for spectral analysis. This requires a high finesse. For *dual* or *triple* systems much lower finesse per etalon can be employed. In practice these finesse values for tunable etalons are typically 20–70 in the visible but in the VUV the finesse values are 5–10. (A finesse value of ∼50 can be assumed as a limiting upper value for etalons, assuming improved technology with $\delta_{\rm rms} \leq 0.3$ nm. For the fixed-gap etalon, the plate flatness and parallelism should be controlled thermally, in order to achieve an effective finesse of ∼50 for the fixed-gap etalon.) For a 10 pm *FWHM*, the FSR is ∼60 pm, which implies multiple etalon systems in order to have a larger *effective* FSR;

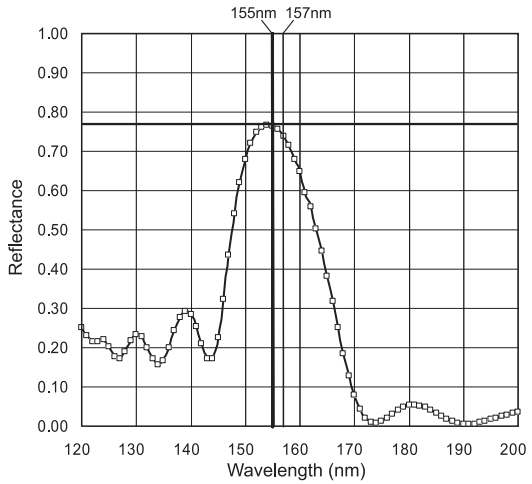

Fig. 12. The Cascade VUV etalon Π-coating spectral profile for the scanning FPI with reflectance at 77% for CIV (155 nm). The vertical wavelength lines for CIV at 155 nm and for the F_2 laser line at 157 nm are shown. The peak reflectance is $R = 0.77$ with corresponding reflectance finesse of $F_R = \pi R^{1/2}/(1-R) = 12$. At the laser line (157 nm), the reflectance is $R = 0.74$ and $F_R = 10.4$.

Fig. 13. Close-up of the VUV FPI etalon assembly with the housing removed. Shown are two of the three curved cantilever springs with the piezoelectric stack beneath. In the center are the MgF_2 etalon with the VUV coatings and, hence, clear in the visible. At the top between the two springs are two capacitance bridges and one reference bridge.

since, these designs are limited by commerical VUV interference filters which have a passband of ≥10 nm.

To insure minimum wavefront distortion after mounting, i.e., minimum mirror wrapping due to mechanical forces, our approach for the mechanical mount is the Hansen mounting (Killeen et al. 1982). This mounting is necessary for orbital observatories since the etalon must be firmly held in place during launch (Figs. 13 and 14). The mount uses a set of longitudinal cantilevered beam springs that are matched to the elastic properties of the etalon spacers. Such a mount provides the necessary stability of the deformation finesse and are standard products of Hovemere.

2.1.4. Spectral range

The wavelength coverage of the VUV FPI must be ∼0.2 nm (Figs. 2 and 7) to be able to observe both lines of CIV. The CIV (154.82, 155.08) emission in the logarithmic middle of the transition region (Fig. 3) is a measure of the heating and dynamics affecting the corona above. Furthermore in order to test the etalon, the reflectance coatings should allow the etalon to scan the molecular F_2 laser line at 157 nm. Therefore, the spectral coverage should be ∼3 nm but limited to this range to allow the spectral passband to perform as a prefilter of parasitic light.

Table 2. Design Parameters for the VUV 10 pm interferometer.

Operating wavelength: $\lambda = 155$ nm
Clear aperture : 25 mm
Coating reflectance: 0.79
Effective reflectance: 0.65
Reflective finesse: $F_R = 7$
Defect finesse: 13
Total finesse: 6
Optical gap: $d = 200$ mm
Free spectral range: 60 pm
Passband width: 10 pm

2.1.5. Optical configuration and aperture

Assuming paraxial ray tracing, the Lagrange optical invariant (the product of the beam aperture and the angle of the oblique chief ray) determines the maximum incident angle of the beam in the interferometer gap ($n = 1$) (Smith 1990). This statement is true for both collimated and telecentric beams assuming that the FPIs are at the position of minimum beam size. For observing typical active regions, the field of view should be FOV∼3 arcmin. For a 300 mm telescope aperture (typical sounding rocket apertures) and a half-diagonal $FOV_{1/2}$ of 1.5 arcmin, the maximum incident angle in a 25 mm etalon is some 12 times larger, or $\alpha \sim 0.3$ degree. For an etalon mounted in a collimated beam, the wavelength shift through the etalon is $\Delta_s\lambda = \alpha^2\ \lambda/2 \sim 2.1$ pm at $\lambda = 155.0$ nm. For a telecentric configuration, the effective passband is

$$FWHM_{\rm eff} = \left[(FWHM)^2 + (\alpha^2\lambda/2)^2\right]^{1/2}.$$

In a telecentric-mounted configuration, the *FWHM* of the etalon will be approached by the system only if $\Delta_s\lambda$ is on the order of *FWHM*. For a 2 pm passband, this would require an etalon aperture of 25 mm for a full 3-arcmin FOV. The effective passband width would be 2.8 pm for a telecentric beam. A collimated system $FWHM_{\rm eff} = 2$ pm width (with a wavelength variation across the field of view) or a telecentric system $FWHM_{\rm eff} = 2.8$ pm (in which etalon artifacts have larger effects on the final image quality and which broadens the passband) can be considered. However for a 10 pm filter, etalon passband is $FWHM_{\rm eff} = 10.2$ pm, hence a FOV of ∼4 arcmin can be considered for this larger passband.

The telecentric configuration avoids the strong variation of wavelength across the FOV of a collimated beam design. A negative aspect of a telecentric configuration is that it produces a slight pupil apodization as a function of wavelength (the Beckers effect, von der Lühe & Kentischer 2000). The spectral passband change across the etalon pupil causes a Point Spread Function (PSF) variation (dependent on the etalon tuning), which leads to Doppler velocity errors for solar spectral lines. In an F/256 configuration the velocity errors were calculated to be less than 10 m s^{-1}. For large F-number configurations, the analysis implies that a telecentric beam can be used with a minimum pupil apodization effect. Furthermore, the analysis by Scharmer (2005) shows that the phase errors introduced by a slower telecentric system can be largely compensated by refocusing. Scharmer points out that the effects of inhomogene-

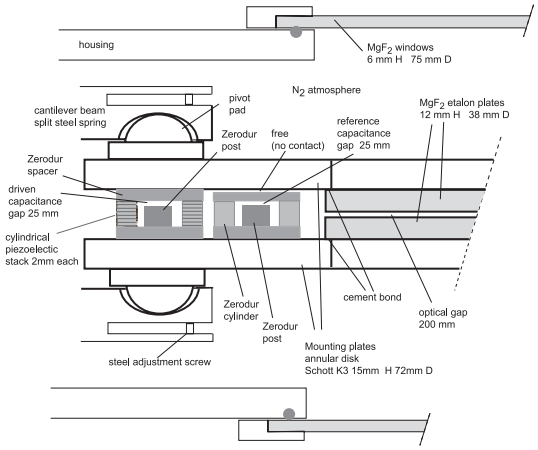

Fig. 14. Schematic of the piezoelectric-tunable, capacitance-stabilized VUV FP etalon. Each piezoelectric driver is matched with a capacitor made of metallized Zerodur post providing electronic tuning of the optical gap. The MgF_2 etalon plates are cemented to mounting plates that are held by a Hansen cantilever beam. The MgF_2 housing window holds a pure N_2 atmosphere for transmittance at 155 nm. The reflectance Π-coatings cover 30 mm area centered on the etalons. The annular holes in the glass mounting plates are 35 mm diameter.

ity in the optical cavity must be considered in the analysis and the ratio of the gap cavities and the reflectance are important. Scharmer (2005) concludes that the telecentric configuration is the preferred configuration for high-imaging quality.

Multiple reflections within a system of etalons produce ghost images which can be a problem. Methods to ameliorate the ghost images can be found in literature (e.g., Scharmer 2006; Tritschler et al. 2002; McKay 1999; Kentischer et al. 1998). These methods include: (1) tilting the elations slightly and adding a wedge angle to the exterior etalon surfaces, (2) adding an adsorption plate between etalon pairs, (3) employ telecentric configurations so the ghost image are far out of focus, and (4) adding antireflection coatings. Cascades Optical Corporation has developed a antireflection coating of MgF_2 and LaF_3 that reduces the reflection to a few tenths of percent ($R < 0.005$). If the incident beam is polarized, then using one 45-degree prefilter mirror between each etalon pair followed by MgF_2 quarter wave-plate, the inter-etalon reflections could be reduced. The success of these various options will be experimentally investigated and reported in a later paper.

2.1.6. Blocking filters – prefilters

In designing the VUV FPI for operation, a prefilter (or blocking filter) is necessary to insure the elimination of the parasitic orders of the multiple etalons, since a single dielectric filter cannot be made to have the passband and transmission requirements. Typical commercial filters in the 155 nm range have a transmission of 5% and a bandpass of 10 nm. However, a set of mirrors with dielectric Π-coatings provides an acceptable prefilter. A system of four mirrors with VUV dielectric is shown in Fig. 8. The blocking filter system is consistent with the following requirements: (a) to obtain the Zeeman sensitive CIV lines at 154.82 and 155.08 and the laboratory surrogate F_2 line; (b) to have a filter transmittance of >80% (i.e., total 4-mirror reflectance of >80%) and off-band transmittance of $\sim 10^{-5}$; (c) to have an effective full width at half maximum (*FWHM*) of ~3 nm (to optimize the etalon trade-offs); (d) to operate with a telescope which has a half-diagonal $FOV_{1/2}$ of 3–4 arcmin (allowing

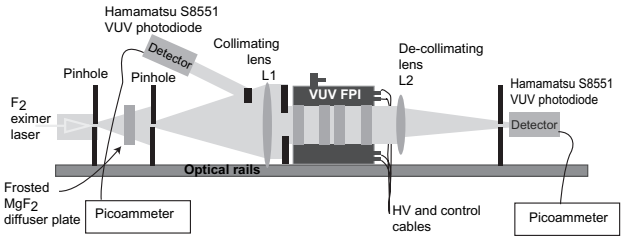

Fig. 15. Schematic of the test setup for the VUV FPI for supplying a collimated beam using either the pinholes or removing the pinholes and using the slowly diverging laser beam. An aperture stop, in front of the FPI, determines the beam size through the etalon.

50–75% of all solar active regions to fit within the FOV)(Tang et al. 1984); (e) to operate with a 300 mm telescope aperture; and (f.) to operate in a beam so that the spectral tuning and transmission profile are uniform over the field of view.

The VUV, dielectric-high-reflectance (DHR) prefilter is based on the work of M. Zukic where each mirror is a Π-multilayer. In this approach, the light is reflected from each high-low refractive layer pair in phase as compared to quarter-wave stacks in which each layer is reflected in phase (Zukic & Torr 1995). Each element is, typically, 25 dielectric multilayer stacks of LiF_3 (high) and MgF_2 (low). The wavelengths long of the region of interest are primarily absorbed or transmitted by the materials in the dielectric stack. The wavelengths short of the region of interest are primarily absorbed by the substrate on the reflective elements. However, there is a limited number of materials that are transmitting (small extinction coefficient) in this region, and, of those transmitting materials many become less transparent in orbit due to solarization or radiation (Zukic et al. (1990a,b) and Keffer et al. (1994). Detailed prefilter designs have been given by Zukic et al. (1993).

Figure 19 shows the Ultraviolet Imager spectral transmission which used reflections from three mirrors. A four-mirror CIV prefilter could be similar but with improve peak transmission. The four mirrors would be employed such that the two reflecting planes of a mirror pair are titled orthognal to the other mirror pair. This arrangement (illustrated in Fig. 8) provides a linear-polarization free optical arrangement since both the s and p-components are reduced equally as prescribed by the Fresnel equations.

3. Development and construction

This section will discuss our development and construction of a CIV interferometer and cover (i) the VUV dielectric coatings and film-induced stress on the etalon plates, (ii) the fixed-gap etalon to evaluate the plates and coatings, (iv) the construction of the PZT tunable etalon, (iv) the control system, and (v) visible light test. The final verification and results are discussed in Sect. 4.

3.1. Etalon plates

At 155 nm there are three transmitting substances for the etalon plates: calcium fluoride, lithium fluoride and magnesium fluoride. Following the Wüsler et al. (2000) study, we selected crystalline MgF_2 since it has been polished successfully and has less hydroscopicity than LiF_3 and are much less sensitive to shock than CaF_2. Within the 155 nm range, MgF_2 shows no induced optical degradation when irradiated with a beam simulating a high-energy space environment (i.e., 10^{14} e/cm^2 at 2 Mev)

(Heath & Sacher 1966); whereas LiF shows strong optical degradations. The internal transmission of MgF_2 at 155 nm is excellent, with typical transmittance of $T > 80{-}50\%$ for 2–50 mm thicknesses; the main loss is surface reflections. Magnesium fluoride is a birefringent optical crystal and any polarized beam should be aligned along the optical axis to avoid birefringent effects. The windows of the interferometer N_2 housing are also MgF_2 and were cut so that the C-axis was perpendicular to the polished surface. The polishing of MgF_2 plates to a plate finesse of better than 25 in the VUV was achieved (cf., Thorne & Howells 1998). ICOS polished two pairs of MgF_2 etalon plates to a curvature of less than $\lambda/150$ at $\lambda = 633$ nm (Fig. 11).

3.2. Dielectric Etalon Coatings

The two viable coatings for the VUV etalon are (i) metallic film with MgF_2 overcoat and (ii) an all dielectric multi-layer stack (Bruner et al. 1997). The aluminum coatings with a magnesium fluoride overcoat have the advantages of very low stress for the two soft layers, provide broad-band reflectance, and have a short coating time which reduces the final cost of the coatings. Their disadvantages are the difficulty of reproducibility due to Al_2O_3 developing on the exposed boundary during coating, variations in reflectivity and absorption, and the extreme handling care to avoid damaging the soft surfaces. The best performance for aluminum is a reflectance of $R = 0.73$ and a loss of $L = 0.08$.

The second and better alternative is our design choice of an all dielectric stack with the advantages of durable, high reflectance coatings. Their absorptances are a third of that of aluminum and improves $T_{\max}$ by ∼2 fold. The resulting transmission profile (Fig. 12) provides a broad passband prefilter (∼20 nm). The dielectric coating disadvantages are i) they require a minimum of ∼25 coating runs and hence are higher cost coatings; ii) they must employ low-stress ion deposition coatings, and iii) need to employ Π-filter technology to minimize the absorption.

The coatings that were used on the etalons are Π-multilayers of high-low (LiF_3-MgF_2) refractive layer pairs (Zukic et al. 1993). The Π-filters improve the reflectivity and lower the absorption by decreasing the relative thickness of the higher index layer while retaining each high-low optical stack thickness to $\lambda/2$ (Zukic & Torr 1990, 1995). Because of the increased reflectivity, the number of Π-stacks is less and the absorption further reduced. Decreasing the LiF_3/MgF_2 paires allows lower absorptance, and the ion deposition provides low stress coatings. This makes use of the 10^{-4} value of the MgF_2 extinction coefficient in the VUV (Zukic 1990a). The coating requirements were $R = 0.77 \pm 0.03$ at 153–157 nm. The final test showed that the reflectance was within ±0.01 of 0.77. A series of coating models were run to optimize the absorptance, transmittance, bandpass, and layers. The reflectance decreases with the H/L-ratio and the passband increases with H/L ratio. The maximum reflectance and passband increases with the number of layers in the coatings (Zukic & Torr 1995). The resulting H/L-ratio was ∼1/4, with the optical thickness $H = \lambda/10$ for LiF_3 and $L = 4\lambda/10$ for MgF_2. The 25 layer Π-coating design was optimized with absorptance of $L = 0.008$.

3.2.1. Film-induced stress

Dielectric interference coatings can impose substantial stress on Fabry-Perot etalon plates from differential thermal expansions of the coating deposited at elevated temperatures. Although mir-

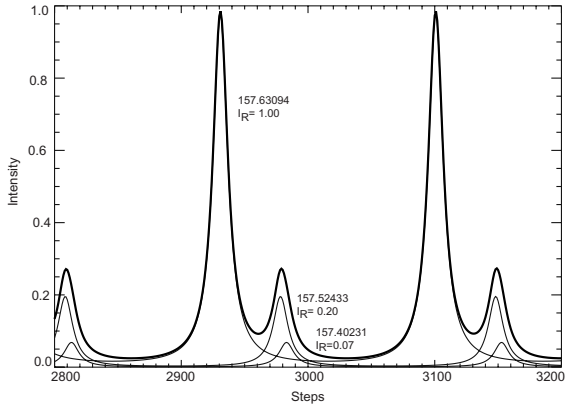

Fig. 16. A simulated profile scan of the F_2 laser lines over two orders with etalon parameters: $d = 200$ um, $R = 0.77$, $FSR = 61$ pm, $FWHM = 5.1$ pm, maximum displacement = 1.9 μm. and step resolution = 1/4096. I_R is the relative F_2 line intensity lines (Sansonetti et al. 2001). The three F_2 lines, from different orders, appear in the same FSR.

Table 3. Triple and dual-etalon and prefilter characteristics.

	Scanning HRI	Scanning HRI	Static LRI	Prefilter 4-mirrors
Refractive Index	1.0	1.0	1.0	
Aperture (mm)	35	35	35	35
Reflectance	0.790	0.790	0.947	0.950
Order	9001	2571	44	
Gap distance (μm)	697	200	3.42	
Coating finesse	13	13	59	
FSR (nm)	0.017	0.60	3.43	
$FWHM$ (pm)	2	10	60	3500
Contrast ratio	73	73	1350	

cocrystaline material structures might produce strains (Ristau et al. 2000), the bulk thermal expansion coefficient of LiF_3 and MgF_2 ∼ (1.4×10^{-5} K^{-1}) are similar. Because stress can warp the etalons and reduce the effective finesse, we evaluated the ion-deposited Π-coatings by using a pair of identical MgF_2 etalons. We have confirmed the suitability of the coatings by showing that the film stress is low. This was accomplished by coating a pair of CIV etalons and then overcoating the elatons with with Al/Ag, for higher reflectance in the visible. A fixed-gap Fabry-Perot/Fizeau unit was then assembled and tested optically with a HeNe laser interferometer.

3.3. Etalon assembly

The initial efforts has been to build and test a 10 pm scanning HRI. The etalon uses MgF_2 plates. Because of the difficulty of providing anti-reflection (AR) coatings at 155 nm and possibly stressing the plates, the plates were given no AR coatings. The single etalon equations for the central wavelength λ_o, FSR, finesse , and passband ($FWHM$) used for the preliminary design are given by: (i) $\lambda_o = 155$ nm, (ii) $FSR = 60$ pm, (iii) $F_R \approx -\pi/\ln R = 11$, and (iv) $FWHM = FSR/F_R = 7$ pm, assuming no optical defects (Vaughan 1989). The design parameters are shown in Table 3 for a dual and triple etalon system.

The construction of this first tunable VUV etalon used annular ring mounting plates of Schott K3 glass to hold the MgF_2 etalon plates (Fig. 14). The MgF_2 plates were cemented onto angular rings of Schott K3 glass which was selected to match

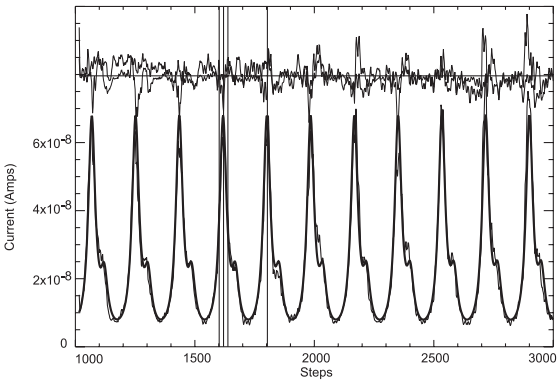

Fig. 17. The diode current of an 11 order scan of the interferometer (Table 5, scan C). With the F_2 laser at low pressure, this scan shows the effect of the lower intensity laser lines. Curve fitting the total data set results in a FSR = 0.062 nm, $FHWM$ = 12.302 pm, and step size = 0.430 nm. The upper insert plots the noise (thin) and the difference between the data and fitted curve (thick). The vertical lines at ~1600 mark the $FWHM$ spectral width and profile center; the vertical line at ~1700 marks the profile center of the next order.

the temperature coefficient of expansion of MgF_2 ($\alpha_{\rm MgF}$ = 8.48−13.7 × 10^{-6}/K and α_{K3} = 8.30 × 10^{-6}/K). The mounting plates allow a minimum thickness for the magnesium fluoride etalons.

The K3 mounting plates are held by a modified Hansen mount as improved by Hovemere Ltd. Each mounting plate is cemented to pads on the cantilever Invar spring beam of split design (Killeen et al. 1982). The spring design allows adjustment of tension to match the piezoelectric forces by adjusting the split separation.

The piezoelectric stacks are PZT-8 (lead zirconate titanate). The applied voltage is controlled by a capacitance stabilized control system such that each of the three piezoelectric stacks has a pair of corresponding readout capacitance bridges and a reference bridge. A transformer ratio bridge and phase-sensitive demodulators provide the feedback system (cf., Jones & Richards 1973); this allows tilt and piston shift motion control of the etalons by a LabView-based software control system. The PZTs allow a variable range of the gap distance of 1.8 μm with 1/4098 digital resolution across or a spatial gap resoluton of 0.4 nm.

3.3.1. Visible light test

Although the reflectance in the visible is less than 2%, we were able to perform tests of the etalon system using a stabilized HeNe laser. For the HeNe laser, the VUV FPI observations for a step range of 500–3000 is fitted with an Airy function (with loss fixed at 0.03) by minimizing the OPD (gap distance), the reflectivity, the step size scale, and the input amplitude using a least squares (Powell) method. The time at each etalon position = 200 ms, hence the total scan time was ~8 min. The results were: the free spectral range FSR = 1.00 nm, OPD d = 200.01019 microns, reflectance R = 1.219%, and distance per step Δd = 0.437 pm. Using the fitted function, the ratio of Imax/Imin was 1.0458 which gives a reflectance R = 0.0112. This visible light test allowed the parallelism parameters for the PZT controllers to be determined.

Table 4. Diode cross-calibration data.

Diode D1	Diode D2	D1/D2
21.48 μA	22.04 μA	0.975
83.0 nA	83.3 nA	0.998
	Average Ratio	0.986

4. Experiment and verification

4.1. Measurements

The Π-coatings peak wavelengths of the sample plates and transmittance were measured at the the MSFC VUV spectrophotometric test facility. This facility also measured the reflectance of the test dielectric coatings and the MgF_2 plates in the vacuum ultraviolet wavelength range. In order to minimize the exposure of test optics to contamination, the spectrophotometric system was maintained in a class 1000 clean room and in a stainless steel vacuum chamber. A cryogenic hydrocarbon-free pumping system was used to avoid contamination. The vacuum system operated with a base pressure in the 10^{-7} torr range. For the VUV measurements, a high-pressure arc discharge deuterium lamp was used as the source in the 115–370 nm range. A 0.2 m vacuum monochromator, with a concave holographic grating (1200 lines/mm) was the source to a 76.2 cm focal length collimating UV enhanced mirror system. This produced a 10.2 cm monochromatic collimated incident beam for our test optics.

To test the etalon assembly HRI (10 pm), we have used the spectral lines obtained from a molecular F_2 eximer laser as a surrogate for CIV. The 157 nm eximer (excited dimer) lasing medium is an excited F_2 diatomic molecule producing ultraviolet pulses. The etalon was scanned using the Lambda Physik LPF220 molecular F_2 eximer laser of the University of Toronto's nanofabrication facility in Ontario, Canada. The interferometer was placed in the optical delivery chamber which consisted of a 2.5 m-long positive-pressure box of N_2. Molecular nitrogen will transmit wavelengths longer than 145 nm, with the underlying continuum cross section of less than 2×10^{-22} cm^2 (Hudson 1971; Samson & Ederer 2000). The pulse laser beam has beam divergence of 3 arcmin × 10 arcmin (or 1 mrad × 3 mrad) and has a repetition rate of 1 to 100 Hz with energy per pulse of ~25 mJ. The principal F_2 line has a 2 pm spectral width ($FWHM$) at He pressure of ~4 atm, the operating pressure of our measurements (Hill et al. 1993). The relative intensity of the weaker F_2 lines is dependent on the pressure and pulse rate of the laser. The effective line finesse is at least greater than $F_L > 15$ assuming that the pressure is less than 8 atm. The angular finesse for a 10 arcmin beam is the ratio of the FSR to the $FWHM$ spread caused by the beam divergence: $F_\alpha = FSR/(\alpha^2\lambda/2) \sim \lambda/nd\alpha^2 > 200$. For the 1 mm pinhole, the divergence angle is much smaller and is the pinhole aperture divided by twice the focal length at λ = 155 nm of the collimation lens): $\alpha \sim 1.0/(2.\times 207) = 1/414$ rad = 0.002 arcmin. Hence either with the pinhole or the normal laser beam divergence, the finesse of the angular spread is insignificant and the main broadening comes from the F_2 line width.

The schematic of the basic test setup for the measurements of the VUV FPI in the nanofabrication facility is shown in Fig. 15. The F_2 laser beam was collimated with a 1 mm pinhole and lens (ISP MgF_2 plano-convex lens 250 mm focal length in the visible) and was also used with its normal divergence. The Si diodes are Hamamatsu's S8852 with a 10 × 10 mm active surface area with a measured quantum efficiency of QE ~ 0.80 at 155.0 nm and QE ~ 0.90 at 157.6 nm (Vest 2004). The diodes have a typ-

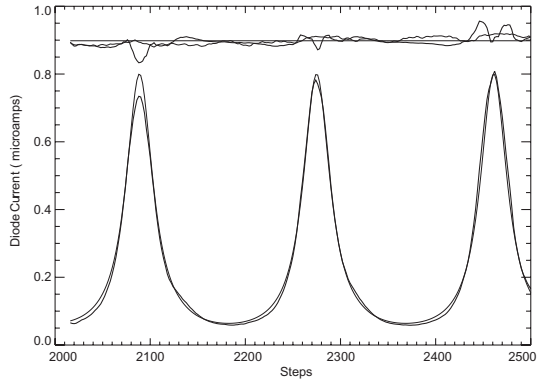

Fig. 18. The results of a 3 order scan of the 157 nm laser (scan A1). A curve of the scan and offset plots of the residual and reference beam are show. Curves in amps with solid line as observed with diode detector using an optical collimated configuration. The thinner curve is derived by fitting the observations with an Airy function with Loss fixed at 0.045 and minimizing OPD (gap distance), reflectivity, step size scale, and input amplitude via a least squares (Powell) method.

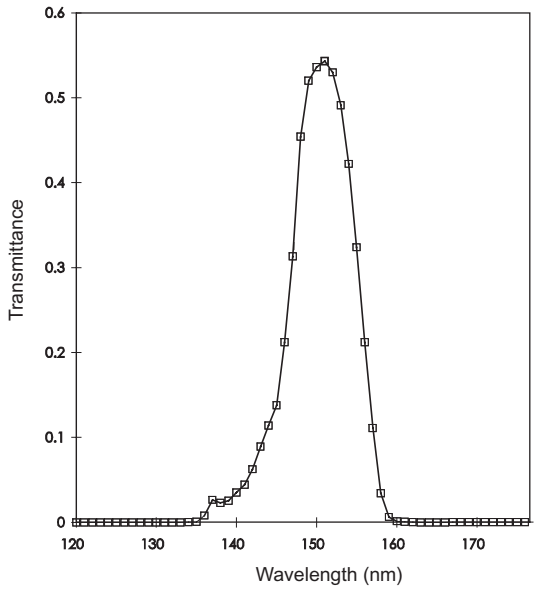

Fig. 19. VUV transmission spectrum of the UVI tri-filter yeilding a peak at 151 nm with a 7.5 nm *FWHM* passband. The prefilter coatings will improve on the UVI profile by an additional reflection and optimization of the individual coating peak transmission. The transmittance is the product of three mirror reflections.

ical rise time of 9 μs and 0.11nA dark current. The diodes were connected to picoammeters (Keithly picoammeter KE6485 for detector D1 and KE6487 for detector D2) for a synchronized record of the two intensities. The detector diode (D1) (on the left of Fig. 15) records the variation of the incident intensity. The detector (D2) recorded the integrated transmittance of the parallel throughput of the etalon. Between the collimating lens (L1) and the entrance window of the interferometer various aperture windows were inserted. The etalon was modulated by the Hovemere capacitance-stablized etalon controller (CSE) which handled the etalon parallelism and sequencing of the etalon position. The sequencing controlled the starting step position, number of steps, the stepping size (typ. 2 pm), and dwell time (typ. 200 ms). The dwell time was set to acquire a measurement and read the data. The overall control system was PC based and programmed under LabView with USB/GBIP interfaces to the picoameters and a USB/RS232 interface to the CSE controller. An external trigger was supplied by the controller to initiate simultaneous 10 multiple readings of the picoammeters.

4.2. Measured etalon parameters

Assuming perfect flatness and normal incident, the interferometer intensity for the triplet F_2 laser lines is the incident intensity I_0 times the sum of the Airy transmission functions for a collimated beam plus dark current/background term $I_{\rm dk}$. As a function of the CSE etalon steps, s, the modulated intensity is:

$$I(\mathrm{s}) = I_0 \sum_{i=1}^{3} \left[T_i \left((1-R+L)^2/(1-R)^2 \right) \times [1 + \left\{ 4R \sin^2(2\pi n d(s)/\lambda_i) \right\} /(1-R)^2]^{-1} \right] + I_{\rm dk}.$$

The least squares difference between the data and this function is minimized using a Powell conjugate gradient method to derive gap distance, d, reflectance R, and distance per step Δd = 0.437 pm, where the OPD gap distance is given as $d = do + \Delta d\ s$. The (λ_i, T_i) values were [(157.63094,1.00), (157.52443,0.20),(157.40231,0.07)]. For the F_2 laser, the weaker two wavelengths are offset from the strongest line by 106.61 pm and 228.63 pm which are greater than the FSR, and hence appear in different orders (see Fig. 16). The T_i values are adjusted for various pressure settings and cadences of the F_2 laser (see Figs. 17 and 18).

The etalon scans were performed and recorded by a LabView program. The F_2 laser pulse rate was 1, 10, or 100 Hz with the laser voltages set at 26 kV, 24 kV, and 24 kV, respectively. At the higher two cadences and lower voltage, the two parasitic F_2 emissions were effectively absent (cf. Fig. 18). In Table 5, the scans A and B were obtained with a cadence of 100 Hz with pinholes removed, and scan C was obtained at 10 Hz with one pinhole being used. In Table 5 where there are two entries for scans A and B, we have assumed two different spectral widths for the F_2 laser ($FWHM$ = 10 and (30) pm). This provides a slight change of 0.7 in the final finesse. Scans A and B are over three orders while scan C is over 6 orders with a higher laser gas pressure. The calculated loss is L = 0.048. In Table 6, we have assumed the laser width of 30 pm, giving the final total finesse of 5.95.

The derived finesse must be corrected for the angular finesse F_α and for the laser line finesse $F_{\rm L}$, however, these are $F_\alpha > 100$ and $F_{\rm L} > 15{-}0$ and do not significantly affect the final finesse. In Table 5 the measured values of the etalon are shown with the correction of the line width of the laser beam assuming both a 15 and 30 pm line width (Hill et al. 1993). Because of slight differences in the coating reflectivity, a finesse correction for wavelength difference is also included by assuming that the defect finesse is constant and only the reflectivity finesse changes.

4.3. Interferometer transmittance

To obtain the interferometer transmittance of the etalon plates a number of operations were needed. First, with a 1 mm beam, the total transmittance of the interferometer with its two entrance windows was measured by placing a photodiode (D1) behind the collimating lens and then removing it and recording across 2 FSR spectral range with the main photodiode (D2), located after the de-collimating lens. Both diodes captured the total beam intensity. The ratio of the input intensity ($I_{\rm input}$), (the intensity

in front of the interferometer), to the output intensity (I_{output}), (the maximum peak intensity behind the interferometer and the decollimating lens) was $I_{input}/I_{output} = 0.12$. Second, the calibration factor between the two photodiodes was applied. The diode calibration was preformed by having both diodes view the same uniformly illumated source surface. The results from the two illumination levels for the cross calibration was determined (Table 4). Third, because of the microroughness of typical MgF_2 interfaces, the main loss of MgF_2 elements occurs at the surfaces and this needs to be corrected. The 155 nm data of West (2004, Fig. 8) for two thicknesses of MgF_2 provide the correction. A thin (2.5 mm) doubled-surface optical element had a loss of 75% while a thick (50 mm) four surface had a loss of 58%. For the MgF_2 elements, the transmission is written as $T = T_s^2(1-T_h \cdot$ thickness), i.e. a product of the surface transmission T_s^2 and the internal transmission $(1 - T_h \cdot$ thickness). Hence the absorption per unit length is $T_h = 1.75\times10^{-3}$ mm^{-1} and the loss per surface is $T_s = .885$. Hence surface effects dominate the transmission loss. The center thickness of the collimating lens is 5.9 mm, the etalons are each 12 mm thick, and the windows are each 7 mm thick. This gives a total path length of 43.9 mm of MgF_2 resulting in an internal absorption of 7.6%. The total percent loss from the two etalons, two windows, and one de-collimating lens (12 surfaces) is a factor of 1/0.272 giving a corrected throughput of 42.6% for the coatings. The forth correction results from the etalon removing the lesser line components of the F_2 laser (see Table 4). This correction factor is 1/0.73. Therefore, the final corrected throughput of the etalon coatings is 58%. This corresponds to an absorption value of $A = 0.048$ for the coatings. Accounting for the throughput by the MgF_2 etalon, the interferometer effective throughput is 34% as a unit.

5. Methodology for a CIV filter

This section discusses the methodology for a development of CIV spectral filter with reference to the development that has been performed and reported here. Clearly, the multiple etalon Fabry Perot interferometer characteristics are based on a tradeoff between having maximum spectral resolution with high throughput and the ability to manufacture a prefilter of minimum passband. The proposed etalon characteristics for a CIV interferometer are shown in Table 2 and Fig. 8. For the fixed-gap etalon, the gap distance is 3.42 μm and tilt tunable. For this small gap-distance along with the fact that the large *FWHM* is 3.5 nm, the etalon can be constructed as a fixed-gap etalon. This fixed-gap design assures that the etalon plates will not touch during launch vibration and simplifies a spacecraft instrument. The second tuning etalon (Fig. 8) has a *FWHM* of ~10 pm to be compatible with the defect finesse. The 10 pm filter design for spaceflight is compatible with the 1/4th line-width criteria. The field of view (FOV) effect on wavelength shift for a telescope aperture and an etalon aperture size was considered and found acceptable for the SUMI telescope but the orbital instrument will depend on the specific mission capabilities and its optical configuration. The top etalon in Fig. 8, a 2 pm *FWHM* interferometer, provides the triple etalon system with high spectral resolution for complete line profiling.

The etalon from our coating test can be refurbished into a fixed-gap (LRI) etalon. The LRI etalon plates need to be repolished and coated with similar high-reflectance ($R = 0.95$, $F_R = 58$) coatings to Figs. 10. The LRI in a fix-gap, thermal control, tilt-tuning assembly will allow selection of a specific spectral order when combined with the prefilter profile. The etalon spacers, mounting supports, and thermal controller for the LHI can be readily provided by current technology. The high finesse is accomplished with the Π-coatings and having the unit as a fixed-gap etalon (Zukic 2000).

Table 5. CIV VUV etalon parameters.

Scan	A1(2)	B1(2)	C
Gap (μm)	201.6	205.2	200.0
Effective reflectivity	0.590	0.561	0.490
Step size (nm)	0.425	0.423	0.430
Aperture size (mm)	2	2	2
FSR (nm)	0.0616	0.0610	0.0620
Measured *FWHM* (pm) at 157 nm	11.56	11.48	12.30
Effective finesse	5.34	5.27	5.05
FWHM of F_2 laser (pm)	30(10)	30 (10)	10
Finesse corrected for F2 laser width	5.43 (5.71)	5.36 (5.63)	5.36
Reflectance finesse			
157 nm ($R = 0.74$)	10.4	10.4	10.4
155 nm ($R = 0.77$)	12.0	12.0	12.0
Defect finesse	6.37 (6.85)	6.25 (6.70)	5.88
Effective finesse at 155 nm (pm)	5.26 (5.95)	5.54 (5.95)	5.55

The four-mirror prefilter design uses the proven tri-filter UVI coatings (cf. Fig. 19). The VUV FPI prefilter can improve on the UVI coatings with a transmittance of ≤80%.

6. Conclusions

The results and design given here demonstrate that a VUV FP interferometer can provide a CIV spectral filter for the solar transition region. This unit can result in a smaller optical system and hence a smaller focal-plane spacecraft instrument that reduces the overall cost as compared to spectrographs. It also allows a higher throughput at high spectral sensitivity, allows short exposures, and improves the magnetic sensitivity of solar magnetographs. The successful development and testing of the VUV FP interferometer will (i) provide new technology for solar science and (ii) allow for solar transition region magnetographs for future space mission and for specific spaceflight TR magnetographs. The investigation of this alternate optical configuration will provide specific opportunities for the CIV VUV FPI for sound rocket experiments using exising telescopes, detectors, and orbiting mission which are now in a instrument definition phase. Figure 20 gives sounding rocket configuration based on using the SUMI 30 cm aperture telescope. This FPI configuration is about a third of the SUMI spectrograph length and mass.

Our results are the following: Two pairs of MgF_2 etalon plates have been polished to better than a $\lambda/150$ at 633 nm or $\lambda/24$ at 155 nm ($F_D > 12$). A primary set of test plates were coated with the designed 77% reflectance at 155 nm. The coatings were stress-free VUV dielectric coatings having low-absorption Π-coatings. These coatings were then applied to the second pair of etalon plates. The tunable interferometer was assembled with MgF_2 plates mounted to annular rings of silica glass of matching CTE in a novel design and was mounted as a piezoelectric-tunable, capacitance-stabilized etalon. The etalon was placed in a Hovemere's Hansen optical mount for low induced mechanical stress. A LabView-based program for the control system was developed to evaluate the interferometer. The evaluation with 157 nm F_2 laser provides the characteristics

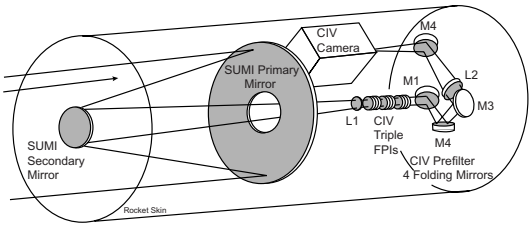

Fig. 20. A sounding rocket configuration of a triple FPI system with the folding mirror prefilters feeding a CIV CCD camera system. The design makes use of the cold-mirror 30cm-aperture telescope for the Solar Ultraviolet Magnetograph Investigation (SUMI, West et al. 2000) which was designed to transmit only the CIV (155 nm) and MgII (280 nm) wavelength bands (*FWHM*∼ 15 - 45 nm).

Table 6. Measured Characteristics of the VUV 10 pm Interferometer.

Operating wavelength: λ = 155 nm
Clear aperture : 25 mm
Coating reflectance: 0.77
Effective reflectance: 0.59
Reflective finesse: $F_{\rm R}$ = 12
Defect finesse: 6.8
Total finesse: 5.9
Optical gap: d = 200 mm
Free spectral range: 61 pm
Passband width: 10 pm
Order: m = 2580
Transmittance: T = 58% (Loss L = 4.2%)

given in Table 2. The result of this program is an operational and robust CIV VUV interferometer.

The specific TR scientific investigations of imaging, doppergraphy, and magnetography have been discussed. The high resolution imaging potential of the transition region by the current set of spacecraft as well as sounding rocket flights is impressive. The study of these images has shown the highly dynamic behavior of the transition region to the limit of spatial resolution. In the VUV, the emission lines are generally optically thin which should allow future spaceflight observations to view down to the scale of the finer physical processes and allow magnetic heating to be understood. However the fine scale features will be associated with short time events since the transition region has very short (seconds) conductive time scales. This requires rapid imaging to avoid smoothing dynamic events.

The configuration of the photospheric and chromosphere-coronal magnetic fields in a stressed active region and a highly sheared low-lying core field is assumed to be enclosed within a more nearly potential arcade of loops at some higher level. Whether the shear decreases with height between the photosphere and chromosphere in such a region, as we might expect from the overall change, has not been observed. The shear might even increase over this lower range. An inversion layer investigation of the magnetic field can show whether the shear increases or decreases with height between the photosphere and chromosphere. Transition region magnetography may find changes in rapidly-evolving active regions as the core fields reconnect to change the shear. This possibility was the prime motivation of the sounding rocket program SUMI/MSFC which through improved technology will extend measurements of the magnetic field higher into the transition region.

A scientific objective of the CIV FPI observations is to characterize the magnetic field in an atmosphere layer of flare locations and determine the 3D magnetic field structure of solar active regions. The radiometry and polarization values show that it is possible but not easy. The HRTS instrument gives the peak line intensity for the two CIV lines as CIV (154.8185 nm) = 2.1 erg cm^{-2} s^{-1} sr^{-1} and CIV (155.0774 nm) = 1.2 erg cm^{-2} s^{-1} sr^{-1} (Roussel-Dupree 1984). The etalon system will need a 2–7 pm spectral resoluton in order to perform the spectral isolation of ∼1/4 of the CIV line width. A polarimeter and camera system will be needed to obtain the appropriate V/I measurements over an active region. The Lande g-factors are $g_{\rm eff}$ = 1.167 (154.82) and $g_{\rm eff}$ = 1.333 (155.08). The 154.82 nm line is about 1.5 times stronger and has an observed width $FWHM \approx 20-39$ pm or Gaussian effective width $\Delta\lambda_E \approx 12-23$ pm. For $\Delta\lambda_E$ = 12 pm, one obtains the normalized Zeeman splitting $\nu_B \approx 6.1\times10^{-4}$ B$_2$, the normalized Stokes-V maximum value $V_{\rm max}/I_p \approx 5.2\times10^{-4}$ B$_2$, and the normalized Stokes-Q, $Q_{\rm max}/I_{\rm p} \approx 8.2\times10^{-8}$. For the field strength of B = 1000 G, the $V_{\rm max}/I_{\rm p}$ = 5.2% and $Q_{\rm max}/I_p$ = 0.008%; hence for a full vector magnetograph, a meter-class space telescope is needed to obtain the full vector field at CIV, but this is a relatively small step and within the state of the art (Gary et al. 2006).

Another scientific objective of the CIV VUV FPI is to provide rapid cadence of the transition region where chromospheric material is being injected from below, where compensating coronal plasma is being injected from above, and where waves and shocks are propagating to heat the corona. The observation of HRTS at 156.07–156.15 nm of CI have shown CI upflow jets (Hoekzema et al. 1997) having blue-shifted events of 15–25 km s^{-1} that last for 40s, whereas most plasma from the lower transition region is blue shifted at 10 km s^{-1} (Solanki & Hammer 2001). The apparent downflows and upflows might be a compression region due to acoustic waves from magnetic heating, or the counter flow might be a consequence of contained chromospheric ejections undergoing temperature changes during their lifetime. Hansteen & Wikstol (1994) point out that the CIV ionization state is highly dependent on velocity, density, and temperature and that rebound shock models might explain the velocity paradox. Solanki & Hammer (2001) states that the ultimate understanding needs more detailed observations which can be provided by Doppler imaging. Doppler imaging will also allow better understanding of traveling waves by analysis of time delays between observations in different levels of the atmosphere. Moreover the energetics of the lower transition region is a key to the heating of the corona and mass loss to the solar wind and the FPI will allow rapid, 2D Dopplergrams in context with TR magnetograms.

Acknowledgements. We thank Dr. David Schiminovich (Space Radiation Laboratory, California Institute of Technology) for making critical VUV reflectivity measurement on etalon coating when the MSFC VUV test facility was under repair. We appreciate greatly the support by Dr. Jianzhao Li (Department of Electrical and Computer Engineering, University of Toronto) for supporting the verification measurements in the F_2 Laser Microfabrication System. We thank Dr. Ken Dere (George Mason University) for supply the HRTS spectral image of CIV. We thank Drs. John M. Davis and James Spann (MSFC/NASA) for their support and encouragement during the development and testing of the VUV interferometer. We appreciate the suggestions of the referee which have improved the paper.

References

Atherton, P. D., Reay, N. K., Ring, J., & Hicks, T. R. 1981, Soc. Photo-Optical Eng., 20, 806

Bartoe, J.-D. F., Brueckner, G. E., Purcell, J. D., & Tousey, R. 1977, Applied Optics, 16, 879

Baskin, S., & Stoner, Jr., J. O. 1975, Atomic Energy Level and Grotrian Diagrams (New York: Elsevier)
Bideau-Méhy, A., Guern, Y., Abjean, R., & Johannin-Gilles, A. 1976, Appl. Opt., 15, 2626
Bideau-Méhy, A., Guern, Y., Abjean, R., & Johannin-Gilles, A. 1980, J. Phys. E: Sci. Instrum., 13, 1159
Bideau-Mehy, A., Guern, Y., & Abjean, R. 1983, J. Phys. Sci. Inst., 17, 255
Bideau-Méhy, A., Guern, Y., Abjean, R., & Johannin-Gilles, A. 1984, J. Phys. Sci. Inst., 17
Borrero, J. M., Solanki, S. K., Bellot Rubio, L. R., Lagg, A., & Mathew, S. K. 2004, A&A, 422, 1093
Bruner, M. E., Wülser, J.-P., Zukic, M., & Hoover, R. B. 1997, Proc. SPIE, 3113, 441
Brueckner, G. E., et al. 1995, Sol. Phys., 162, 311; the issue also includes description of SUMER and UVCS
Chae, J., Wang, H., Lee, C.-Y., et al. 1998, ApJ, 497, L109
Dammasch, I. E., Wilhelm, K., Curdt, W., & Hassler, D. M. 1999, A&A, 346, 285
De Pontieu, B., Tarbell, T. 2002 Bull. AAS, 34, 790
De Pontieu, B., Erdélyi, R., & De Wijn, A. G. 2003, ApJ, 595, L63
DeForest, C. E. 2004, ApJ, 617, L89
Dere, K. P., Bartoe, J.-D., F, & Brueckner, G. E. 1982, ApJ, 259, 366
Dere, K. P., Bartoe, J.-D. F., Brueckner, G. E., et al. 1991, J. Geophys. Res., 96, A6, 9399.
Feldman, U., Widing, K. G., & Warren, H. P. 1999, ApJ, 522, 1133
Gary, G. A. 1990, Mem. Soc. Aston. It., 61, 457
Gary, G. A. 2001, Sol. Phys., 203, 71
Gary, G. A., Balasubramaniam, K. S., & Sigwarth, M. 2003, Proc. SPIE, 4853, 252
Gary, G. A., West, E. A., Rees, D., Zukic, M., Herman, P., & Li, J, 2006, CIV Vacuum Ultraviolet Fabry-Perot Interferometers for Transition-Region Magnetography, ASP Conference Series, in press.
Gontikakis, C., Peter, H., & Dara, H. C. 2003, A&A, 408, 743
Guern, Y., Bideau-Méhu, A., Abjean, R., & Johannin-Gilles, A. 1974, Optics Communicatons, 12, 66
Hagyard, M. J., Gary, G. A., & West, E. A. 1988, The SAMEX Vector Magnetograph, NASA Tech. Memo. 4048
Handy, B. N., Bruner, M. E., Tarbell, T. D., et al. 1998, Sol. Phys., 183, 29
Hansteen, V. H., & Wikstol, O. 1994, Space Sci. Rev, 10, 103
Hays, P. B., & Snell, H. E. 1991, Appl. Opt., 30, 3108
Heath, D. F., & Sacher, P. A. 1966, Appl. Opt., 5, 937
Herman et al. 2001, Proc. SPIE, 4247, 149
Hernandez, G. 1986, Fabry-Perot Interferometers (New York: Cambridge University Press)
Hicks, T. R., Reay, N. K., & Atherton, P. D. 1984, J. Phys. E; Sci. Instrum., 17, 49
Hill, P. C., Herman, P. R., & Sia, R. 1993, J. Appl. Phys., 73, 5274
Hoekzema, N. M., Rutten, R. J., & Cook, J. W. 1997, ApJ, 474, 518
Hudson, R. D. 1971, Rev. Geophys. Space Phys., 9, 305
Jelinsky, P. N., Morrissey, P. F., Malloy, James, M., et al. 2003, Proc. SPIE, 4854, 233
Keffer, C. E., Torr, M. R., Zukic, M., Spann, J. F., Torr, D. G., & Kim, J. 1993, Appl. Opt., 33, 6041
Kentischer, T. J., Schmidt, W., Sigwarth, M., & Uexkull, M. V. 1998, A&A, 340, 569
Killeen, T. L., Hays, P. B., Kenndy, B. C., & Rees, D. 1982, Appl. Opt., 21, 3903
Killeen, T. l. et al. 1999, Proceed. SPIE, 3756, 289
Korendyke, C. M., Vourlidas, A., Cook, J. W., et al. 2001, Sol. Phys., 20, 63
Madjarksa, M. S., & Doyle, J. G. 2003, A&A, 402, 731
McKay, J. A. 1999, Appl. Opt., 38, 5851
McKay, J. A., & Rees, D. J. 2000, Optical Engineering, 39(01), 315
Moore, R. L., & Sterling, A. C. 2005, Initiation of Coronal Mass Ejections, Solar Eruptions and Energetic Particles, ed. N. Gopalswamy, AGU, Washington
Peter, H. 2000, A&A, 360, 1108
Peter, H. 2001, A&A, 374, 1108
Peter, H., Gudiksen, B. V., & Norlund, A. 2004, ApJ, 617, L85
Pietraszewski, C. 2001, Private communications
Porter, J. G., Moore, R. L., Reichmann, E. J., et al. 1987, ApJ, 323, 380
Porter, J. G., & Dere, K. P. 1991, ApJ, 370, 380
Rees, D. 2005, private communication
Roussel-Dupree, R., et al. 1984, ApJ, 278, 428
Ristau, D., Günster, S., Bosch, S., et al. 2000, Appl. Opt., 41, 3196
Samson, J. A., & Ederer, D. L. 2000, Vacuum Ultraviolet Spectroscopy I (N.Y.: Academic Press), Sect. 16.4.3
Scharmer, G. B. 2005, A&A, 446, 1111
Smith, W. J. 2000, Modern Optical Engineering, McGraw-Hill, N.Y., second edition, 47
Solanki, S. K., &, Hammer, R. 2001, The Solar Atmosphere, The Century of Space Science, ed. M. Huber, J. Geiss, & J. Bleeker (New York: Springer), 1065
Stenflo, J. O., Biverot, H., & Stenmark, L. 1976, Appl. Opt., 15, 1188
Tang, F., Howard, R., & Adkins, J. M. 1984, Sol. Phys., 91, 75
Tauger, J. T. 1976, Appl. Opt., 15, 2998
Tarbell, T. D., Handy, B. N., & Judge, P. G. 1999, AAS, 31, 960
Thorne, A. P., & Howells, M. R. 1998, Experimental Methods in the Physical Sciences, Academic Press, 73
Tritschler, A., Schmidt, W., Langhans, W., Langhans, K., & Kentischer, T. 2002, Sol. Phys., 211, 17
Uitenbroek, H. 2001, ApJ, 557, 389
Vest, R. E. 2004, NIST FUV diode calibration report (private communication)
Vaughan, J. M. 1989, The Fabry-Perot Interferometer-History, Theory, Practice and Applications (Philadelphia: Adam Hilger)
von der Lühe, O., & Kentischer, Th. J. 2000, A&A, 146, 499
West, E. A., Porter, J. G., Davis, J. M., et al. 2000, Proc. SPIE, 4139, 350
West, E. A., Porter, J. G., Davis, J. M., et al. 2001, Proc. SPIE, 4498, 101
West, E. A., Porter, J. G., Davis, J. M., et al. 2004, Proc. SPIE 5488, 801
Wülser, J.-P., Rosenberg, A., & Bruner, M. E. 2000 , SPIE Proceed., 4139, 390
Xia, L. D., Popescu, M. D., & Doyle, J. G. 2004, Proceedings of the SOHO 15 Workshop, ESA SP-575, 362.
Zukic, M., Torr, D. F., Spann, J. F., & Torr, M. R. 1990a, Appl. Opt., 29, 28, 4284
Zukic, M., Torr, D. G., Spann, J. F., & Torr, M. R. 1990b, Appl. Opt., 29, 28, 4293
Zukic, M., Torr, D. G., Kim, J., Spann, J. F., & Torr, M. R. 1993, Opt. Eng., 32, 3069
Zukic, M., & Torr, D. G. 1995, Thin Films for Optical Coatings, Thin Films for Optical Coatings, ed. R. E. Hummel, & K. H. Guenther (New York: CRC Press), 79
Zukic, M. 1998, Fabry-Perot Etalons within 120–155 nm FUV Range, private communication